



## Durham E-Theses

---

# *Establishment of Stalagmite $^{232}\text{Th}$ as a Novel Proxy for Dust Flux and the Reconstruction of the Asian Monsoon System during the Late Pleistocene*

VERNIERS, TOM

### How to cite:

---

VERNIERS, TOM (2021) *Establishment of Stalagmite  $^{232}\text{Th}$  as a Novel Proxy for Dust Flux and the Reconstruction of the Asian Monsoon System during the Late Pleistocene*, Durham theses, Durham University. Available at Durham E-Theses Online: <http://etheses.dur.ac.uk/14001/>

### Use policy

---

The full-text may be used and/or reproduced, and given to third parties in any format or medium, without prior permission or charge, for personal research or study, educational, or not-for-profit purposes provided that:

- a full bibliographic reference is made to the original source
- a [link](#) is made to the metadata record in Durham E-Theses
- the full-text is not changed in any way

The full-text must not be sold in any format or medium without the formal permission of the copyright holders.

Please consult the [full Durham E-Theses policy](#) for further details.



Durham  
University

**Establishment of Stalagmite  $^{232}\text{Th}$  as a Novel Proxy for Dust Flux and the  
Reconstruction of the Asian Monsoon System during the Late Pleistocene**

Tom Verniers

Durham University

2020

## Abstract

Aerosols are minute particles that are suspended in the Earth's atmosphere. The variation in composition and size control the impact they have on global climate. This study focuses on mineral dust as a subspecies of aerosols and the reconstruction of its flux in Asia during the late Pleistocene. Stalagmites are upwards growing speleothems (the combined term for stalactites, stalagmites and other cave deposits) composed of calcite or aragonite. Their global distribution, semi-continuous growth and  $^{234}\text{U}/^{230}\text{Th}$  datable laminae make them valuable climate archives. This study establishes a correlation between atmospheric aerosols and stalagmite  $^{232}\text{Th}$  concentrations to take advantage of the absolutely dated stalagmite aliquots and establish a proxy for paleo-dust flux. This proxy is applied to a reconstruction methodology for Asian dust flux during the late Pleistocene. East Asian dust flux and monsoon intensity are critical systems to understand when modelling the effects of future climate change on the region.

194 Asian stalagmite  $^{232}\text{Th}$  records are interpolated and compiled to produce a median Asian  $^{232}\text{Th}$  curve. A high degree of correlation ( $r^2=0.32$ ,  $p < 0.00001$ ,  $n = 213$ ) between this median  $^{232}\text{Th}$  curve and a global sea level curve (taken from Siddal et al., 2003) establishes a climatic control on the  $^{232}\text{Th}$  curve. This curve is evaluated against a Northern Hemisphere ( $65^\circ$ ) summer insolation model, a compiled East Asian stalagmite  $\delta^{18}\text{O}$  record (taken from Cheng et al., 2016), NGRIP  $\delta^{18}\text{O}$  (taken from North Greenland Ice-Core Project Members, 2004) and a Westerlies  $\delta^{18}\text{O}$  record (taken from Cheng et al., 2016).

During a period of low insolation variability (40-20 ka), and subsequent constant monsoon intensity, the correlation between the stalagmite  $^{232}\text{Th}$  and  $\delta^{18}\text{O}$  records decreases noticeably. During this period, stalagmite  $^{232}\text{Th}$  continues tracking regional dust fluxes, but no longer matches the EA stalagmite  $\delta^{18}\text{O}$  record. This period coincides with the occurrence of North Atlantic Dansgaard-Oeschger (D-O) and Heinrich Events, which have been shown to

affect Asian moisture transport and Indian Ocean surface temperatures. Due to the large amount of moisture the EAM sources from the Indian Ocean, these surface temperatures changes are recognizable in the EA stalagmite  $\delta^{18}\text{O}$  record. Because overall monsoon intensity does not change, stalagmite  $^{232}\text{Th}$  does not record D-O events, while stalagmite  $\delta^{18}\text{O}$  does. This creates the decoupling of the two records observed between 40 and 20 ka.

The application of  $^{232}\text{Th}$  as a proxy for Asian dust flux in this study demonstrates its validity as a climate proxy. The potential generation of an absolutely dated dust-flux record reaching back 500kyrs creates the opportunity to use this methodology in future studies of dust flux reconstruction for all regions of the globe.

## Table of Contents:

<b>1.0 Introduction .....</b>	<b>1</b>
1.1 The Role of Aerosols in the Earth's Climate.....	1
1.2 The Use of Stalagmites in Climate Sciences .....	5
1.3 The Social and Economic relevance of the East Asian Monsoon System .....	7
<b>2.0 Methodology.....</b>	<b>10</b>
2.1 Distribution of Stalagmites used in this Study .....	10
2.2 Stalagmite <sup>232</sup> Th and DCMD Correlation.....	11
2.2.1 Stalagmites Disregarded from the <sup>232</sup> Th and DCMD Correlation Plot .....	14
<b>3.0 Results.....</b>	<b>17</b>
3.1 Evaluation of the rigidity of the <sup>232</sup> Th/DCMD correlation curve.....	17
3.2 Examination of hydrological factors contributing to stalagmite <sup>232</sup> Th.....	19
3.3 Using stalagmite <sup>232</sup> Th as a proxy to reconstruct Asian dust flux .....	21
3.4 Interpolation Gap Features .....	23
3.5 Comparison of a compiled <sup>232</sup> Th with a Loess Dust Flux Record .....	24
<b>4.0 Discussion .....</b>	<b>28</b>
4.1 Correlation with global ice volume .....	28
4.2 Analysis of correlation between $\delta^{18}\text{O}$ records and <sup>232</sup> Th concentrations .....	30
4.2.1 East Asian Monsoon Data .....	32
4.2.2 NGRIP $\delta^{18}\text{O}$ Data .....	35
4.2.3 Problematic correlation period .....	37
4.3 Westerlies $\delta^{18}\text{O}$ data .....	42
<b>5.0 Conclusion .....</b>	<b>45</b>
<b>References .....</b>	<b>50</b>
<b>Appendix .....</b>	<b>55</b>
Appendix 1 .....	55
Appendix 2 .....	55
Appendix 3 .....	70
Appendix 4 .....	73
Appendix 5 .....	82

**Compiled Data Set References: Attached Excel File (Verniers000832400-References.xlsx)**

## 1.0 Introduction

This study aims to improve the understanding of the Asian Monsoon systems throughout the last glacial period by establishing stalagmite  $^{232}\text{Th}$  concentration as a novel proxy record for dust flux. Through the reconstruction of Asian dust flux, climate patterns are illuminated and teleconnections between North Atlantic climate events and East Asian climate are explored. Enhanced understanding of these teleconnections allows for a more accurate interpretation of East Asian climate records, such as speleothem  $\delta^{18}\text{O}$  records, and improves our ability to predict future East Asian Monsoon variability in response to continued climate change. This will be vital in managing potential negative impacts of climate change in a region that remains vulnerable to natural disaster threats.

### 1.1 The Role of Aerosols in the Earth's Climate

Aerosols are minute particles suspended in the atmosphere that exert an important control on the planet's climate (Allen, 2017). Aerosols interact both directly and indirectly with the Earth's radiation budget by affecting the atmosphere's radiative flux at both solar and thermal wavelengths (Miller, 2014). However, these impacts are poorly understood due to variety in physical and chemical aerosol composition, size, the complexity of their interactions and the large spatial and temporal variability of emissions and dispersions (Albani, 2018).

Aerosols in the top of the atmosphere directly influence the radiation budget by absorbing and reflecting solar radiation. Composition and size of aerosol particles control whether specific species have a net positive (black carbon) or negative (sulfates) radiative forcing (Albani, 2018). Aerosols in the lower levels of the atmosphere can indirectly influence the earth's energy budget by affecting cloud and particle size (Allen, 2017).

Through analysis from lidar and the radiosonde observations, Mikami et al. (2006) also found that dust particles acted as nucleation sites for ice particles at the ice-saturated region of the atmosphere. By acting as cloud condensation and ice nuclei, aerosols affect cloud lifetime and albedo, impacting how clouds reflect and absorb terrestrial radiation (Allen, 2017). These effects cause the local climate to redistribute energy and moisture. An example of this is how absorbing aerosols reduce relative humidity by impacting cloud formation via heating (Albini, 2018).

Radiative forcing in the top of the atmosphere is the primary way in which aerosols perturb surface air temperatures. This is especially prevalent in areas frequently mixed by deep convection. Elevated aerosol concentrations lead to increased dimming of the ground surface and a decrease in surface evaporation. For this reason, models associate increased atmospheric dust with reduced global precipitation. However, counter examples can be found on a smaller scale where greater shortwave absorption by dust particles increases ground surface evaporation and therefore local precipitation. These interactions between atmospheric aerosols and regional climate (precipitation, surface wind speed, vegetation etc.) create a feedback mechanism linking back to the aerosol concentration (Miller, 2014).

Aerosols do not only affect the global and regional climates when suspended in the atmosphere. Surface albedos, such as snow, can be greatly reduced by the deposition of aerosol species like black carbon and mineral dust (Albini, 2018). Aerosols also impact the terrestrial and marine biospheres. Wind-blown sediment deposition in the oceans provide essential minerals such as iron and phosphorous, a lack of which results in poor biomass production and the formation of high nutrient, low chlorophyll (HNLC) zones. It has been suggested, by John Martin's *Iron Hypothesis*, that increased dust supply to such zones during glacial periods removed the lack of iron as limiting factor and boosted biomass production. This resulted in the removal of atmospheric CO<sub>2</sub> and its storage in the deep oceans (Stoll, 2020). Not only are

aerosols a control on biomass production but land vegetation also plays an important role as a primary source of aerosols. Atmospherically suspended viruses, bacteria, fungal spores, pollen, plant debris and algae, as well as black carbon produced by vegetation fires, are all classified as aerosols and have an impact on the climate (Albini, 2018).

Aerosol optical depth (AOD) is an often cited, dimensionless metric used to represent the amount of atmospheric aerosols present. In their memorandum for the MERRA-2 aerosol assimilation system, Randal et al. (2016) present the following derivation for AOD:

$$AOD = y = \sum_{z,i} x_i \times b_{ext,i}(RH) \times \partial z$$

Where  $x_i$  is the concentration of 15 species  $i$  (dust (5 size bins), sea salt (5 size bins), hydrophobic and hydrophilic black and organic carbon and sulfate (SO<sub>4</sub>)).  $\partial z$  is the layer thickness and  $b_{ext,i}(RH)$  is the species-specific extinction coefficient derived from Mie-theory (Randal, 2016).

The emission, distribution and deposition of aerosols are interlinked in a feedback loop with the hydrological cycle, vegetation growth, surface winds and changing climatic conditions. Therefore, it is critical to understand these interlinked systems in all of their complexity, when considering how the addition of anthropogenic aerosols over the past century, and future years, will impact climatic changes. Developing an understanding of the connections between atmospheric aerosols and climate will allow for improved simulations and constructions of global Earth System Models (Albini, 2018). Chen et al. (2018) simulated the total dust emissions on a global scale between 2007 and 2010. 81% of global dust emissions were produced by natural sources, while the remaining 19% was contributed by anthropogenic sources (Chen et al., 2018). Due to the major role dust plays in the Earth's hydrological cycle,



carbon cycle and energy budget, its reconstruction is a critical component to understanding the Earth's climate history. Understanding the role that anthropogenic dust sources play in today's climate could be pivotal in developing future climate models.

Paleoclimatology is the study of past climates using proxy records where direct measurements are not available. Palaeoclimate proxies are physical, chemical and biological materials preserved within the geologic record (in paleoclimate archives) that can be analysed and correlated with climate or environmental parameters in the modern world (What Are Proxy Records, 2020). Important qualities of a proxy record include the range of time it spans across and its resolution. Different proxy records can be found in different archives, including tree rings, ice cores, lacustrine/ocean/continental sediments and stalagmites.

Ice cores provide an extensive record of multiple aerosol species such as: mineral dust, sea salts, sulfur, nitrogen species and carbonaceous aerosols. However, this climate archive is spatially limited to high and low latitudes throughout geological history. Carbonaceous aerosols can also be recorded in charcoal found in lacustrine sediments, peats and soils. This study is specifically interested in mineral dust as a subspecies of aerosols. The pure form of mineral dust is almost insoluble, making it a stable tracer that can be preserved in a variety of archives such as: ice cores, marine sediments and loess deposits (Albini, 2018). The most direct measurement of dust is by measuring the insoluble dust number and volume concentration using a Coulter or laser optical counter. These measurements, combined with dated deposition windows, allow the dust mass accumulation rates (DMAR) to be derived. DMAR can also be derived in marine sediments by measuring the mass of residual sediment after the removal of opal and carbonates, as well as the measurement of geochemical lithogenic proxies concentrations (such as; Al, Ti,  $^{232}\text{Th}$  and  $^4\text{He}$ ). Particle size distributions and provenance fingerprinting are two other properties that are commonly derived from marine sediments and loess deposits (this is done with laser optical counters and radiogenic isotope composition,

respectively), to reconstruct paleo dust fluxes. In loess deposits DMAR is derived from radiocarbon or luminescence dated soil horizons (Újvári, 2010). These methods are subject to large uncertainties and are limited in their range, often requiring age-model-derivations and correlations with relevant sedimentary sequences to be used in combination with these methods (An et al., 1985). Uncertainties in soil horizon dates translate to their respective DMAR calculations. As a result, loess record dust flux reconstructions are limited in their temporal coverage and are associated with high levels of uncertainty due to the poor constraint of relevant dates. The establishment of stalagmites as an archive for a new viable aerosol proxy;  $^{232}\text{Th}$  concentrations, alleviates these constraints while extending the temporal coverage up to 500 ka.

## 1.2 The Use of Stalagmites in Climate Sciences

Stalagmites are a type of speleothem most commonly found in limestone caves. Speleothems are most commonly formed of  $\text{CaCO}_3$  polymorphs calcite or aragonite. Rain or ground water flowing through limestone bedrock picks up dissolved calcium carbonate and carbon dioxide. This calcium carbonate and carbon dioxide react to form calcium bicarbonate. As the water enters the cave chamber through small cracks in the cave ceiling, the lower cave atmosphere  $\text{pCO}_2$  causes water to degas and precipitate calcium bicarbonate back out (Magiera, 2019). Over time a stalactite begins to form as calcium carbonate is deposited repeatedly to form a small mound hanging from the cave ceiling. Water dripping down from stalactites onto the cave floor can degas further, leading to the precipitation of calcium carbonate layers growing upwards, called stalagmites. This stalagmite will continue to grow until it merges with its opposite stalactite to form a column formation. The shape of a stalagmite can vary from a candle (linear and narrow) to a dome or flowstone shape. The morphology is determined by

the variability in the drip rate and the distance from the tip of the feeding stalactite (Frisia, 2019).

The slow, but often continuous, buildup of carbonate layers over time allows stalagmite deposits to record climate signals such as the  $\delta^{18}\text{O}$  (‰) signal of the rainwater that drips from the tip of the overhanging stalactite (Skinner, 2019). Stalagmite aliquots that contain ppb-ppm levels of uranium can be dated by  $^{238}\text{U}$ - $^{234}\text{U}$ - $^{230}\text{Th}$  and  $^{235}\text{U}$ - $^{231}\text{Pa}$  disequilibrium techniques (Dorale, 2004). This method allows a precise growth history to be established for stalagmites and provides a reliable chronology for climate proxies preserved in its laminae.

Unlike uranium, thorium is not soluble and cannot be transported or deposited authigenically by groundwater as the speleothem forms. It is therefore assumed that no initial  $^{230}\text{Th}$  is present in the sample and that any  $^{230}\text{Th}$  measured is a product of the alpha decay of uranium.  $^{232}\text{Th}$  is not part of the  $^{238}\text{U}$ - $^{234}\text{U}$ - $^{230}\text{Th}$  decay chain and therefore any  $^{232}\text{Th}$  in a stalagmite is considered to be representative of detrital material flushed into the cave (Wong, 2015). Thorium isotope  $^{232}\text{Th}$  content is measured and used as an analog to determine allogenic initial  $^{230}\text{Th}$  concentrations and subsequently correct and gauge the accuracy of the aliquot date (Hellstrom, 2006). As such every  $^{234}\text{U}$ - $^{230}\text{Th}$  dated speleothem aliquot has an associated  $^{232}\text{Th}$  concentration.

Because of their precise chronologies and plethora of proxy records, speleothems have played an important role in climate science and the reconstruction of past climates. The global terrestrial distribution of speleothems, as well as their semi continuous deposition, have allowed the creation of a global and temporally distributed proxy dataset invaluable in climate science (Wong and Breecker, 2015).

The high levels of uncertainty associated with each of the methods and natural aerosol archives discussed in section 1.1 means that there is a lack of a reliable paleo-dust archives that are both spatially and temporally distributed. This study uses a multi-stalagmite approach to

reconstruct paleo dust fluxes through examining  $^{232}\text{Th}$  concentrations in stalagmites.  $^{232}\text{Th}$  is applied as a proxy for the amount of detrital contamination of a stalagmite during growth. Detrital components of stalagmites have previously been attributed to material flushed into the cave site by ground water. However, this study demonstrates that  $^{232}\text{Th}$  concentrations could be representative of air born detrital material blown into the cave and settling on top of growing speleothem laminae. The demonstration of a correlation between  $^{232}\text{Th}$  concentrations (recorded in parts per trillion (ppt)), measured as part of the  $^{234}\text{U}$ - $^{230}\text{Th}$  dating process, and mean local dust column mass density values (taken as an indication of dustiness) establishes the validity of  $^{232}\text{Th}$  as a proxy for atmospherically suspended dust aerosols. This study goes on to construct and interpret a compiled Asian  $^{232}\text{Th}$  curve, which is interpreted as a proxy for Asian dust flux and contextualized through a comparison to East Asian Monsoon records. The importance of our understanding of this monsoon system is detailed in the section below.

### 1.3 The Social and Economic relevance of the East Asian Monsoon System

The East Asian Monsoon (EAM) is one of two main subdivisions of the Asian Monsoon system, the other being the Indian Monsoon. The EAM system is driven by the differential heating between the Asian continent and ocean surface waters. The monsoonal flow carries evaporated moisture from the Indian and Pacific Oceans onto the continent. The initial establishment of the EAM remains debated. Hypotheses vary between the EAM beginning in the late Miocene, ca 7-8 Ma, or much earlier than that; in the early Miocene (Liu et al., 2009). The early Miocene appearance of the EAM is supported by a variety of palaeobotanical and lithological evidence. C4 plant type occurrence in the South China sea region as early as 20 Ma and mammalian faunas found in northern Thailand between 16 to 14 Ma both suggest a warm, wet climate. This is supported by lithological evidence from Miocene loess-paleosol sequence at Qinan and the western Loess plateau of China (Sun and Wang, 2005).

The impact of anthropogenically driven climate change over the past centuries on the variability of monsoon rainfall in Asia is critical to understand. Asia is the most densely populated region in the world, with 147 inhabitants per square kilometer (Duffin, 2019). Although Asia has seen large amounts of economic growth over the previous decades the region is still home to half of the world's extreme poor, and issues such as undernourishment, food security and infrastructure remain serious concerns moving forward (FAO, 2018). Climate variability in the region can have serious consequences with intermittent flooding of some regions affecting financial, human, infrastructure and food security factors.

A westward shift has been observed in the Indian Monsoon since the 1970s, and although overall precipitation volumes are observed at 70% of normal volume, topography has affected the intensity of rainfall in other regions (Loo et al., 2015). Flooding frequency has increased since the 1970s (Coenraads, 2006). However, the majority of floods in Southeast Asia are associated with the EAM, costing lives and creating extensive property damage, such as in the Philippines and Thailand in 2012 (Loo et al., 2015).

These shifts in the Indian Monsoon do not only affect the Indian subcontinent but also influence the variability of rainfall and the onset of the EAM. An average delay of 15 days has been predicted for the annual onset of the EAM in the future (Loo et al., 2015). Monsoon variability is not only an important factor for the region in terms of flooding risk. Due to a lack of sufficient irrigation systems many regions in South East Asia (SEA) rely on monsoonal rainfall to fill aquifers and wells for the remainder of the year (Solace Global, 2018).

Furthermore, increased rainfall variability and intensity increases the demand for sufficient drainage systems and effective prewarning systems for flooding dangers and events, such as the examples listed above. According to the International Disaster Database more than 1,200 people lost their lives and more than 40 million were impacted by a relatively average monsoon season in 2018 (Solace Global, 2018). Monsoon rainwater is not only used for

agriculture but also in the production of electricity. Hydropower output has quadrupled in SEA since 2000 (IHA, 2020). Delays, or variability, in summer monsoon rainfall could therefore greatly impact the region's economy. A lack of water resources leads to a drop in agricultural production, and a consequential increase in food imports, as well as the increased cost of power production. These factors predominantly affect rural regions where intermittent blackouts become more common (Solace Global, 2018).

“Understanding the shift and predicting changing trends of monsoon may be central to managing the floods that impact on millions of people, damage to lives and property, destruction of ecology and farmlands and the long-term effect on food security.” (Loo et al., 2015). A variety of proxies have previously been used to reconstruct different features and processes within the monsoon. Lithogenic tracers, clay minerals and trace elements (archived in hemipelagic sediments) are just three proxies that have been used to reconstruct wind directions. Planktonic, coral and speleothem  $\delta^{18}\text{O}$  records have been used to reconstruct monsoon-driven precipitation (Wang, 2005). Section 1.2 discussed the limitations of proxies used to reconstruct dust flux and paleo aridity. This study uses the uranium-thorium dating capabilities of stalagmites to create a more reliable chronology of dust flux through time, building a better understanding of monsoonal trends in Asia during the late Pleistocene.

## 2.0 Methodology

This section establishes stalagmite  $^{232}\text{Th}$  concentrations as a viable proxy for palaeo dust-flux. This is done by demonstrating the correlation between recent stalagmite  $^{232}\text{Th}$  concentrations and relevant Dust Column Mass Density (DCMD) data by producing a  $^{232}\text{Th}$ /DCMD correlation curve (Figure 1). The section also discusses the stalagmites compiled, utilized and disqualified from the production of this curve.

### 2.1 Distribution of Stalagmites used in this Study

Hundreds of stalagmites have been harvested and sampled worldwide since Allison (1923) first published a paper on speleothem morphology. This study compiles the corrected ages and associated  $^{232}\text{Th}$  values of 435 stalagmites, distributed globally (Figure 1). Areas of high density include SEA and Europe. Northern Africa and central Australia have noticeably poorer coverage. Appendix 1 clarifies the spatial distribution by number of stalagmites per

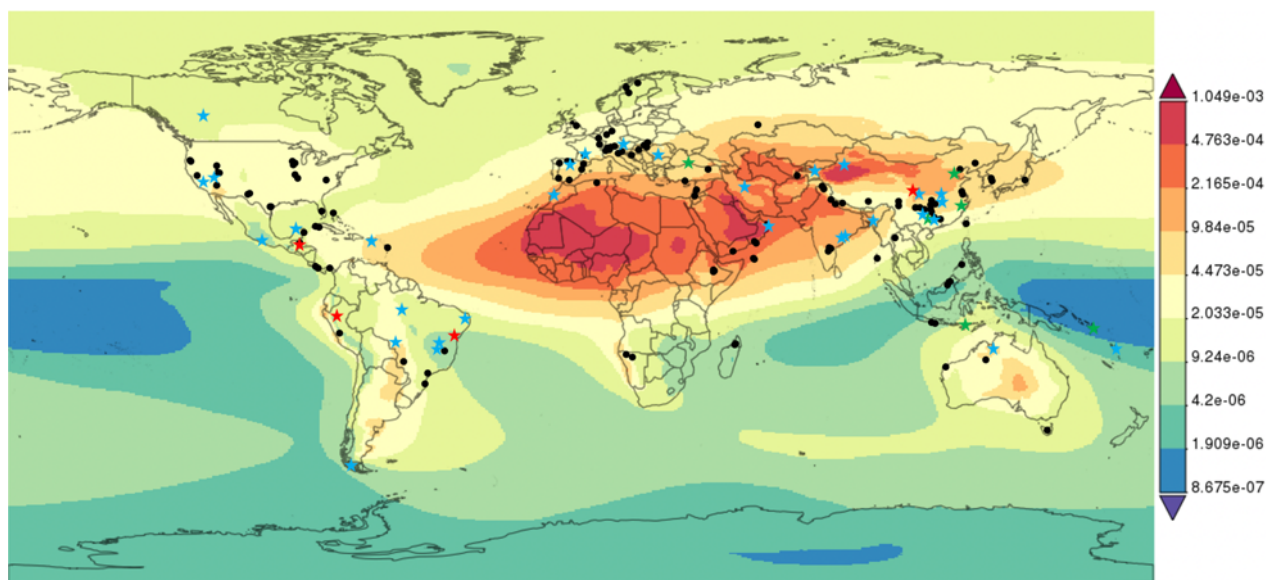


Figure 1 demonstrates the global distribution of stalagmites collected for this study. Stalagmites marked with a star symbol are used in the correlation curve. Blue stars indicate single stalagmites, red stars indicate compiled cave data and green stars highlights caves where multiple stalagmites were combined to form a cave data point. Stalagmites marked by black circles are not used in the correlation curve. The base map shading illustrates mean Dust Column Mass Density ( $\text{kg m}^{-2}$ ) between January 2000 and 2020. Data is sourced from the public EarthData Giovanni NASA database.

continent, excluding Antarctica. The stalagmite distribution is excellent and instrumental to this study as well as to the construction of a new climate archive.

Stalagmite growth is correlated to temperature and the amount of carbon dioxide available in the soil (Borsato, 2015). A fundamental requirement of stalagmite growth is the input of meteoric water to the karst, thus explaining the lack of stalagmite occurrence in hyper-arid regions, such as Saharan Africa and central Australia. Arid regions such as these are also linked to high quantities of atmospheric mineral dust aerosols, as well as carbonaceous aerosols from regular vegetation fires. The low number of records found in these regions mean there is a lack of high  $^{232}\text{Th}$  concentration and high DCMD data points available. This limitation is discussed later when evaluating the reliability of the correlation curve.

## 2.2 Stalagmite $^{232}\text{Th}$ and DCMD Correlation

A correlation curve demonstrates the relation between modern day DCMD and recent stalagmite  $^{232}\text{Th}$  concentrations (Figure 2). DCMD data was taken from the *Modern-Era Retrospective analysis for Research and Applications version 2* (MERRA-2) dataset, a NASA atmospheric reanalysis for the satellite era using the Goddard Earth Observing System Model, Version 5 (GEOS-5) with its Atmospheric Data Assimilation System (ADAS), version 5.12 (Global Modeling and Assimilation Office, 2015). The data was extracted as an area-averaged time series of a monthly temporal resolution, for an area of  $1^\circ$  squared around each stalagmite. A mean value for the last 20 years was then produced and used in the correlation plot. Recent  $^{232}\text{Th}$  data is defined as mean concentration values measured in stalagmite layers in the last 500 years BP (see Appendix 2 for tabled values).

Figure 1 shows a time averaged map of DCMD data measured between January of 2000 and March of 2020. Warmer colors indicate regions of elevated DCMD. Randle et al. provided a memorandum for the MERRA-2 aerosol assimilation system in which they present *Equation*



*I*, used to derive AOD. This study is interested in the correlation between mineral dust and  $^{232}\text{Th}$ , hence the decision was made to use DCMD instead of AOD to remove the effects of sea salt, carbon, nitrogen and sulfate aerosols on the correlation curve.

To establish a correlation between modern DCMD and recent  $^{232}\text{Th}$  data, stalagmites with age records within the last 500 years were filtered from the dataset. Each stalagmite used has a minimum of 2 dates within the last 500 years BP, allowing for the calculation of a mean value. 71 Stalagmites fulfilled this basic criterion. When calculating a mean  $^{232}\text{Th}$  concentration (ppt) over the last 500 years, any values further than one standard deviation away from the mean were discarded. This minimizes the effects of miscellaneous data produced from singular events such as floods or dust storms. Where multiple stalagmites within the same cave met these criteria, both stalagmites were used. In this case a single mean value was calculated for the cave as a whole by compiling the two stalagmite data sets. The same procedure, as was applied to singular stalagmites, was followed, when calculating compiled mean  $^{232}\text{Th}$  values. The following caves contain compiled data from the listed stalagmites (also see green stars in Figure 1):

- Dongge Cave, China: D4 and DX1
- Shihua Cave, China: LS-9602 and TS-9701
- Shennong Cave, China: SN20 and SN4
- Liang Luar Cave, Indonesia: LR06-B1 and LR06-B3
- Sofular Cave, Turkey: So-1 and So-10

Similarly, caves within close enough proximity to have overlapping source areas of DCMD data were compiled into singular data points. These include the following stalagmites:

- ELC-A, Sha-2, PAL 3, PAL4 and CAS-D taken from El Condor, Shatuca, Palestina and Cascayunga Caves, in Peru, respectively.

- Gu-Xi-1 and YOK-G, respectively taken from Xibalba and Yok Balum Caves, in Belize.
- LD12, TR5 and DV2, respectively taken from Lapa Doce, Torrinha Cave and Diva de Maura Caves, in Brazil.
- HY1, HY3 and WX42B, respectively taken from Huangye and Wanxiang Caves, in China.

Although this method ignores the impact of controls such as cave geometry, ventilation and water flux, it is applied to the data set because in order to support the hypothesized relation between the two variables, a single DCMD data point must be correlated with a single  $^{232}\text{Th}$  concentration. Because these stalagmites interact with the same atmosphere, containing the same amount of suspended aerosol particles, their  $^{232}\text{Th}$  concentrations should reflect this. This is shown by the respective standard deviations found within the compiled data (Appendix 3).

Beyond compiled stalagmite data within the same caves and overlapping DCMD data, a further 16 stalagmites were disqualified from the correlation curve. These are discussed below. As a result, the final correlation data set is comprised of 49 caves and a total of 55 stalagmites. The curve demonstrates a strong  $R^2$  correlation coefficient of 0.63 ( $p < 0.00001$ ,  $n = 49$ ) between mean  $^{232}\text{Th}$  concentrations (ppt) and mean DCMD ( $\text{kg m}^{-2}$ ) values since 2000 (Figure 2). A further evaluation of the validity of this correlation can be found below, in section 3.1.

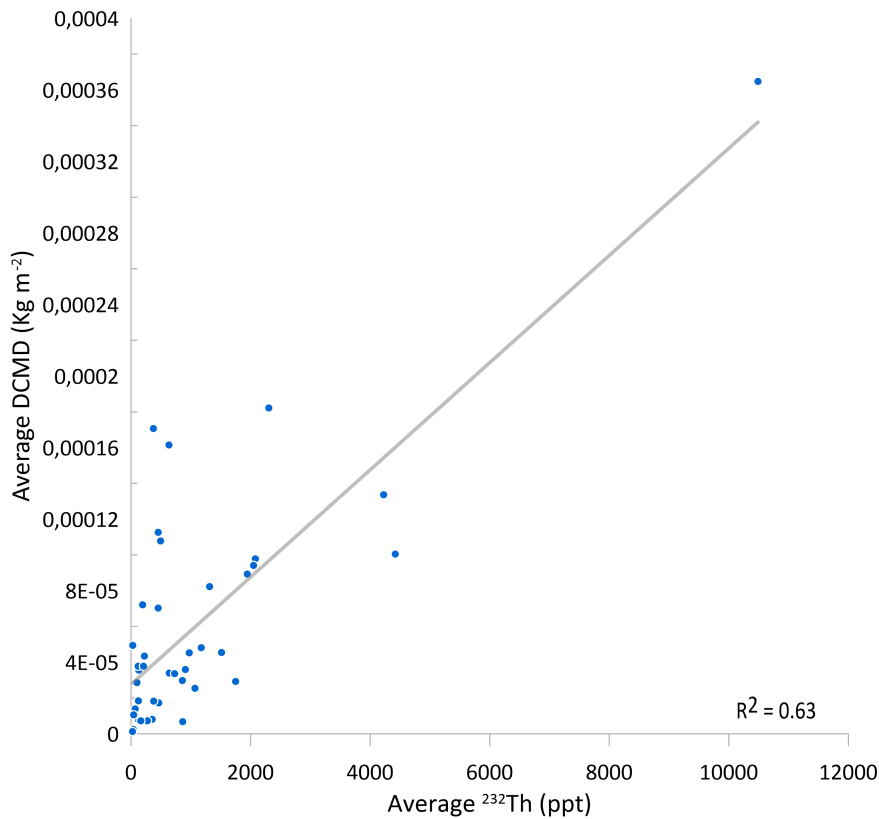


Figure 2 illustrates the positive correlation between mean  $^{232}\text{Th}$  values over the last 500 years and mean, modern DCMD values taken from an area of  $1^\circ$  of latitude and longitude squared around the cave site.

### 2.2.1 Stalagmites Disregarded from the $^{232}\text{Th}$ and DCMD Correlation Plot

Although a broad-brush approach was used to create an Asian  $^{232}\text{Th}$  curve (Figure 5), the 71 stalagmites that fulfilled the two basic criteria to be included in the correlation curve were more heavily scrutinized. Another 16 stalagmites were removed from the correlation curve based on a number of criteria described below. To establish a correlation between atmospherically suspended dust aerosols and stalagmite  $^{232}\text{Th}$  concentrations the data included in the correlation curve need to reliably represent these two variables. As such these criteria have been designed to create a higher standard for inclusion than that of the median Asian  $^{232}\text{Th}$  curve (discussed in section 3.3). More detailed information on the disqualification of each of the following stalagmites can be found in Appendix 4.

The following three stalagmites were removed from the correlation curve because isochrons were required to constrain their initial detrital content or age:

- AB-2 taken from Anjohibe Cave, Madagascar
- BA03 taken from Bukit Assam Cave, Malaysia
- FR0510-1 taken from Furong Cave, China

Additionally, nine stalagmites were removed due to inconsistent staining, porosity or discontinuous coloration throughout laminae. These stalagmites include the following:

- PGH-1 taken from Panigarh Cave, India
- DP1 taken from Dante Cave, Namibia
- 20120824-13 taken from Yelang Cave, China
- MC01 taken from Macal Chasm, Belize
- TUL taken from Chulerasim Cave, India
- IFK1 taken from Ifoulki Cave, Morocco
- ZJD-21 taken from Zhijin Cave, China
- P00-H1 taken from Huagapo Cave, Peru
- C11 taken from Cueva del Cobre, Spain

Stalagmite LH2, taken from a collapsed sink in Lianhua Cave in China, was also removed from the plot. Lianhua cave was discovered during roadworks in 2006 and had previously been completely sealed off. As a result, the cave could not interact with the outside atmosphere and data taken from its stalagmites would not be reflective of the relationship between  $^{232}\text{Th}$  and atmospheric aerosol concentrations.

Stalagmite ALH06 was also removed from the correlation curve. This stalagmite was found in the Pau d'Alho Cave in Brazil and used in a study investigating the linkage between

speleothem and soil magnetism, by Jaqueto et al. (2016). The magnetite data extracted from ALHO6 formed a tight cluster and overlap the field of detrital magnetite (on an MDF/DP plot). Furthermore, magnetic data obtained on soils and cave sediments are identical in acquisition curves of IRM and ARM (Jaqueto, 2016). For this reason, we believe that  $^{232}\text{Th}$  concentrations measured in stalagmite ALHO6 are not representative of atmospherically entrained dust but instead originate from local soils. Subsequently, the stalagmite has been removed from the correlation curve.

Finally, two stalagmites were removed due to dating errors or age reversals. Large dating errors in stalagmite PP1 (taken from the Pink Panther Cave in New Mexico, USA) meant that the archive could not guarantee multiple data points within the last 500 years, disqualifying the stalagmite based on one of the two basic criteria. Similarly, two large age reversals at the top of stalagmite S3 (taken from the Kahf Defore Cave in Oman) suggest that it is not a reliable stalagmite that can guarantee a sufficient number of data points in the last 500 years. S3 was also removed from the correlation curve.

This level of scrutiny should be applied to all stalagmites incorporated into a compiled stalagmite  $^{232}\text{Th}$  curve. However, this goes beyond the scope of this study and instead it is limited to the stalagmites which satisfy the two basic criteria required to be relevant to the correlation curve. Pearson and Spearman correlation plots including the removed stalagmites mentioned above can be found in Appendix 5. In conclusion, figure 2 makes a reliable case that  $^{232}\text{Th}$  concentrations in stalagmite aliquots can be used as a proxy for dust flux at the time of their deposition.

### 3.0 Results

This section supports the  $^{232}\text{Th}/\text{DCMD}$  correlation curve presented in chapter 2 (Figure 2) through the production of a Spearman's coefficient plot (Figure 3) and by analyzing the role played by hydrological factors in stalagmite  $^{232}\text{Th}$  concentrations (Figure 4).  $^{232}\text{Th}$  is then applied as a dust flux proxy and a compiled Asian stalagmite  $^{232}\text{Th}$  curve is produced (Figure 5). Strengths and weaknesses of the applied methodology are discussed and highlighted in a comparison between a stalagmite  $^{232}\text{Th}$  and a loess dust flux record (Figure 7).

#### 3.1 Evaluation of the rigidity of the $^{232}\text{Th}/\text{DCMD}$ correlation curve

The linear line of best fit produced for the  $^{232}\text{Th}/\text{DCMD}$  correlation curve has a coefficient of 0.63, indicating a very strong, positive correlation between the two variables ( $p < 0.00001$ ,  $n = 49$ ). This firmly establishes  $^{232}\text{Th}$  as a viable proxy for atmospherically suspended mineral dust aerosols.

However, it could be argued that this value is highly dependent on data from the H12 stalagmite, taken from Hoti Cave, and the corresponding DCMD data ( $^{232}\text{Th}$  concentration of 10,488 ppt and DCMD of  $3.65\text{E-}4 \text{ kg m}^{-2}$ ). Although this is a valid concern, it can be explained by a bias found in data availability. H12 is the only stalagmite on the correlation curve with a  $^{232}\text{Th}$  concentration above 4500 ppt.  $^{232}\text{Th}$  concentrations used in this study come from  $^{234}\text{U}$ - $^{230}\text{Th}$  dated stalagmite aliquots, which were partially selected on their  $^{232}\text{Th}$  concentrations; the lower the concentration the more accurately the aliquot can be processed. Hence, there is a distinct lack of data available for aliquots with more than 2000 ppt of  $^{232}\text{Th}$  (Figure 2). Additionally, annual rainfall above a consistent threshold is a key controlling factor on stalagmite growth. High DCMD values are associated with arid regions, where there is limited ground water flux and therefore limited stalagmite growth. This is evident from Figure 1, and the lack of representation for stalagmites found in areas such as Saharan Africa and central Australia. When stalagmites are found in these regions, they have most likely grown during

wetter climate conditions (suggesting less atmospherically suspended dust aerosols) and upon harvesting and studying these speleothems, aliquots with the least amount of  $^{232}\text{Th}$  are selected. This double bias results in the data distribution seen in Figure 2. This study assumes that additional data collected from stalagmites found in arid climates and aliquots with higher  $^{232}\text{Th}$  concentrations would fill the observed data gap.

Nevertheless, the  $^{232}\text{Th}/\text{DCMD}$  correlation is still significant and statistically robust, a conclusion that is supported by the calculation of a Spearman's Coefficient with an  $R^2$  value of 0.37 (Figure 3).

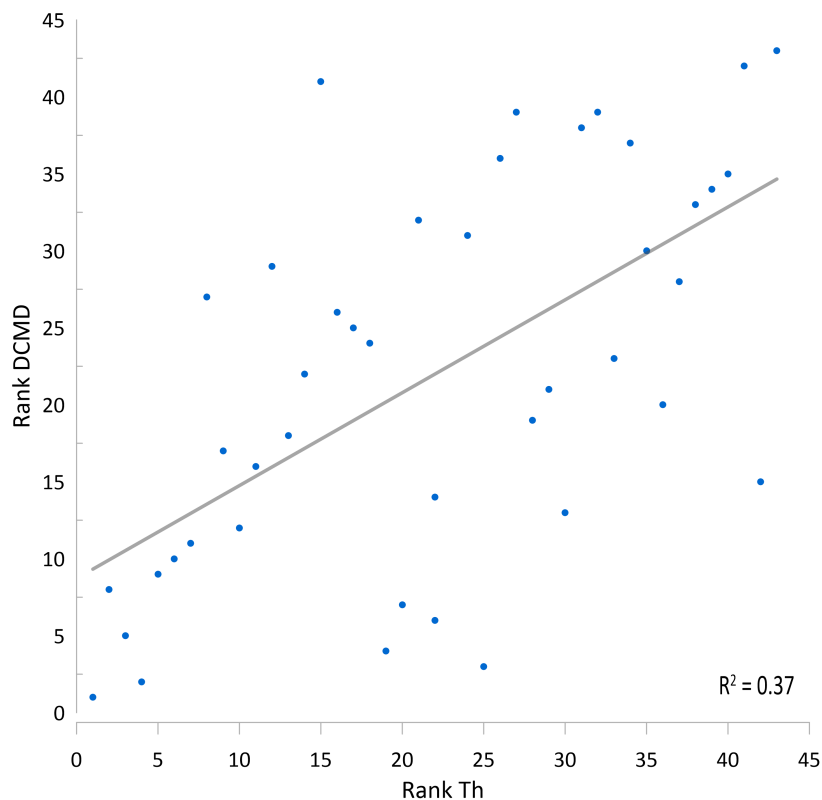


Figure 3. A Spearman's Coefficient plot of modern DCMD and recent mean  $^{232}\text{Th}$  concentrations.

This  $R^2$  value is produced by ranking the mean  $^{232}\text{Th}$  concentration and DCMD data of each data point, in descending order within each data set, and plotting these rank values against each other. This methodology reflects the extent to which an increase in one variable (DCMD) is associated with an increase in another variable ( $^{232}\text{Th}$  concentration), rather than the absolute values of each data point pair. This removes the influence of single data points on the

correlation (Statistics.Laerd, n.d.). A one-tailed statistical significance analysis produces a directional  $\alpha$  value of  $<0.0005$ . The T-table used in this methodology was taken from Ramsey (1989) who produced Edgeworth approximations for  $N>18$  with no error greater than 0.002 in the critical values. The analysis using this table suggests that the identified correlation is highly significant and that there is less than a 0.05% chance that this correlation is a coincidence.

### 3.2 Examination of hydrological factors contributing to stalagmite $^{232}\text{Th}$

As discussed in section 1.2, the  $^{234}\text{U}/^{230}\text{Th}$  dating methodology functions on the principle assumption that a sample contains no initial  $^{230}\text{Th}$ . However, speleothems are never pure calcite or aragonite and often contain impurities, such as detrital particles. These particles (of dust, soil or other detrital debris) contain amounts of thorium. The  $^{230}\text{Th}/^{232}\text{Th}$  isotopic ratio of crustal material is  $5 \times 10^6$  (Hellstrom, 2006). Therefore, the known  $^{232}\text{Th}$  concentration can be used to estimate the initial  $^{230}\text{Th}$  concentration of a sample.

Chapter 2 and section 3.1 have shown that  $^{232}\text{Th}$  concentrations are linked to DCMD values, suggesting that externally sourced detrital dust blown into the cave is the source for any initial thorium. An alternative hypothesis is that detrital material is flushed into the cave by rainwater and contaminates growing speleothems with high thorium concentration containing impurities. Additional hydrological factors could include changes to drip-water pathways, which may produce isotopic signals not directly related to climate (Shimpf *et al.*, 2011). Although this study does not discount local hydrology as a factor in changing stalagmite  $^{232}\text{Th}$  concentrations, it does suggest that it is not the dominant factor. A plot of modern stalagmite  $^{232}\text{Th}$  versus recent Total Surface Precipitation (TSP) values expresses a very weak ( $r^2 = 0.04$ ,  $p = 0.785$ ,  $n = 49$ ) correlation between the two variables (Figure 4a).



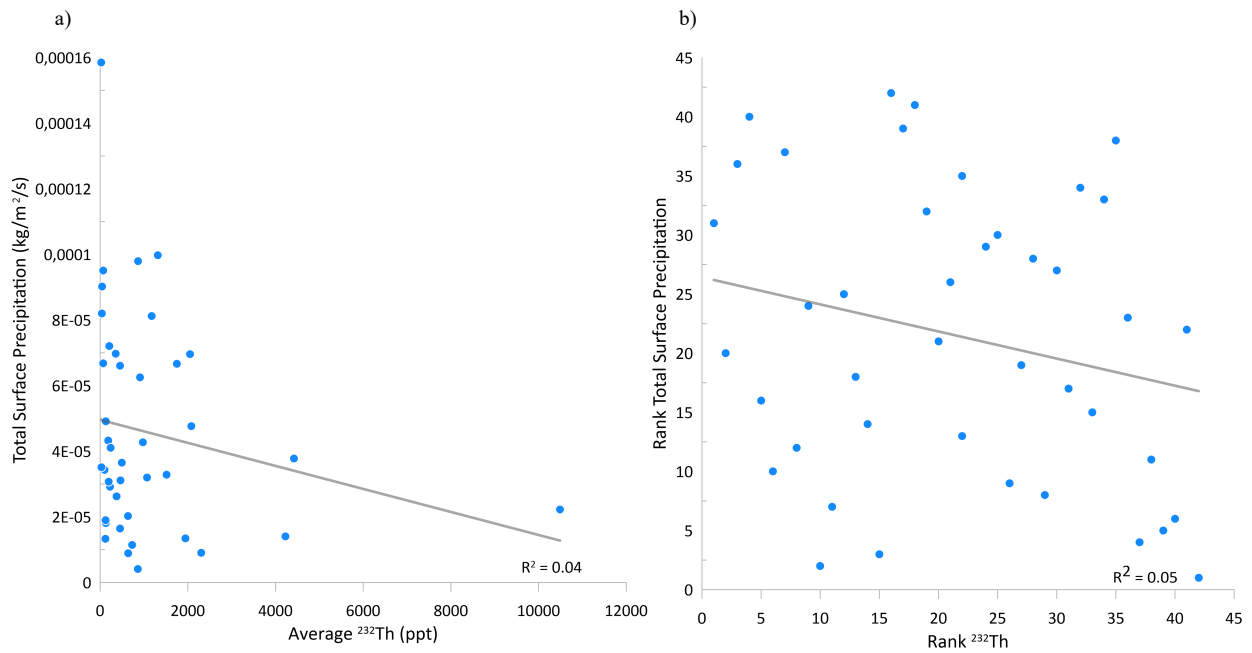


Figure 4a plots mean total surface precipitation (since January 2000) against mean  $^{232}\text{Th}$  concentrations. Figure 4b plots total surface precipitation against  $^{232}\text{Th}$  concentrations as ranked within their respective data sets to produce a Spearman's plot.

The same 55 stalagmites, and their mean  $^{232}\text{Th}$  concentrations (in ppt) are used in this plot as in the DCMD correlation curve. To stay consistent with the production of the DCMD correlation curve, TSP data was taken from the MERRA-2 dataset (publicly available on the giovanni.gsfc.nasa.gov website). A mean TSP value was produced for an area of  $1^\circ$  squared around each stalagmite, from monthly values recorded since the 1<sup>st</sup> of January 2000. Following the same methodology allows for a direct comparison between the correlations between  $^{232}\text{Th}$  and DCMD or TSP (figure 4).

These plots support the conclusion that  $^{232}\text{Th}$  concentrations in stalagmite laminae are an accurate proxy for local atmospheric aerosol concentrations and not influenced by changes in precipitation volume.  $R^2$  values of 0.04 ( $p = 0.785$ ,  $n = 49$ ) and 0.05 (Figures 4a and 4b respectively) demonstrated a slight, negative correlation between stalagmite  $^{232}\text{Th}$  concentrations and precipitation variability. A one-tailed calculation of the statistical significance of Spearman's coefficient, using the same t-table as in section 3.1, produces an  $\alpha$  value larger than 0.25, the correlation can therefore be regarded as insignificant.

### 3.3 Using stalagmite $^{232}\text{Th}$ as a proxy to reconstruct Asian dust flux

Sections 2.2, 3.1 and 3.2 all strongly support stalagmite  $^{232}\text{Th}$  as a valid proxy for atmospherically suspended mineral dust aerosols. To produce a continuous reconstruction of Asian dust flux, 194 stalagmite records were compiled into one curve (Figure 5a). Individual records from these Asian stalagmites were interpolated at a decadal resolution, using the application PAST. Several factors may reduce the reliability of stalagmites as a proxy archive for atmospheric aerosol concentrations, including stalagmite distance from the cave entrance, cave accessibility, chamber size and shape as well as the quality of the system's ventilation. Besides cave geometry and atmospheric controls, there are also key factors that control stalagmite growth to acknowledge. These factors include: the flux of water, the  $\text{CO}_2$  saturation of drip water relative to the cave atmosphere and cave air temperature (Mariethoz, 2012).

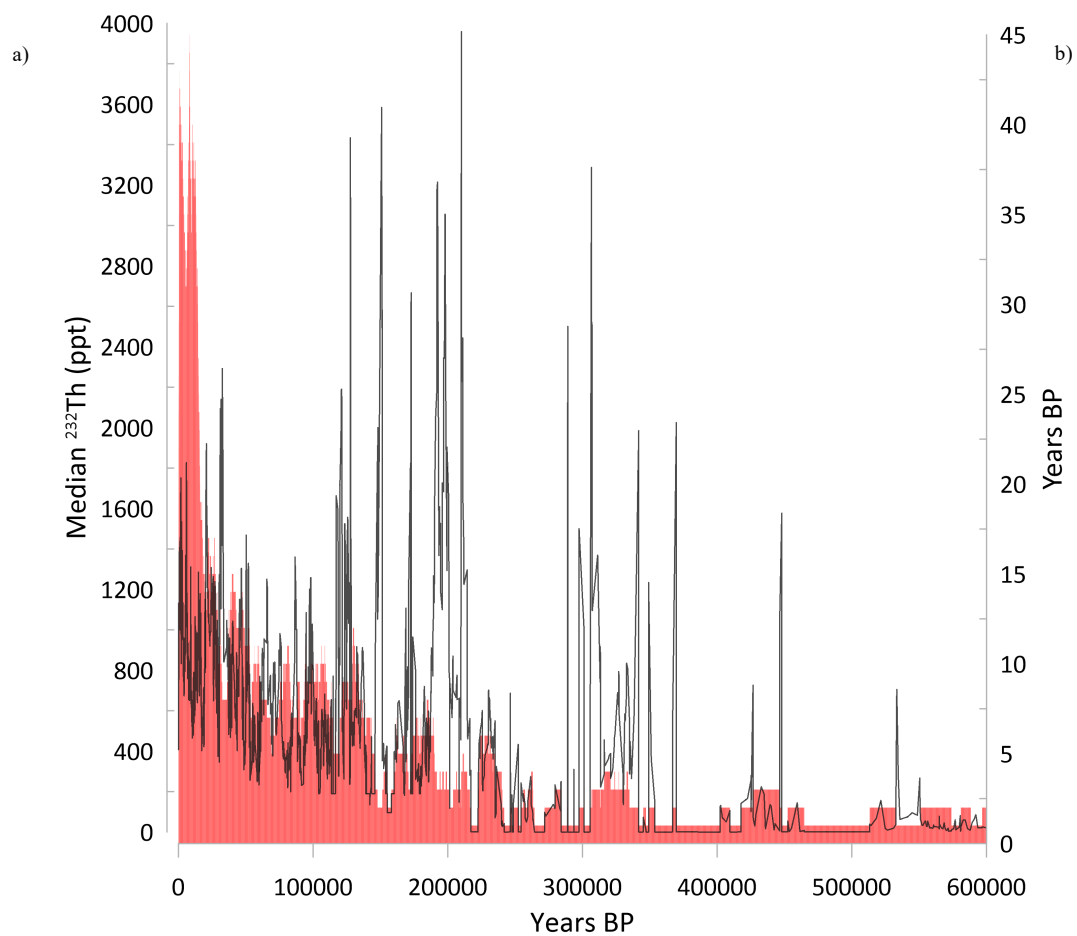


Figure 5a) the black line illustrates a median  $^{232}\text{Th}$  value from a compiled stalagmite record, stretching back to 500 ka. Figure 5b) the red bar chart is a histogram of the number of records used to calculate each median value plotted in figure 5a.

Although these are all relevant controls, their consideration is beyond the scope of this project. A broad-brush approach is applied in this project and cave dynamics were not used when discounting stalagmites from the construction of an Asian stalagmite  $^{232}\text{Th}$  record.

Growth hiatuses of more than 5,000 years in a stalagmite's record were not interpolated across. Gaps of this length in measured data points were deemed too large to assume a constant climate that could be linearly interpolated. Following the interpolation of each individual stalagmite record, a median value was taken for each decade. This value was calculated from the stalagmites with available data for each decade. A median value was used instead of a mean value to negate the impact of data points with anomalously high  $^{232}\text{Th}$  concentrations (Appendix 6 illustrates a time series based on mean  $^{232}\text{Th}$  values, as well as the upper and lower limits of the 95% confidence interval). These values could be the consequence of singular events such as dust storms or cave flooding events and would skew mean values without being representative of regional climate trends.

A histogram of the number of records used in the calculation of each decadal median is shown to highlight the reliability of the median  $^{232}\text{Th}$  curve (Figure 6b). A wider variety and larger number of input data points produce a well-rounded median value that is more reflective of regional climate trends. The exponential decrease in the number of records available during older intervals demonstrates the need for increased data collection for this method to be developed further. Due to this limitation this study focuses on the late Pleistocene period. However, because the methodology uses uranium/thorium disequilibrium dating techniques, the potential is there to produce a record extending back to 500 ka; considerably increased data availability is needed to achieve this.

### 3.4 Interpolation Gap Features

A linear interpolation model was selected for the methodology described in section 3.3 due to the correlation coefficients produced from the linear lines of best fit in Figures 1 and 2. These plots indicate that a linear interpolation model is most appropriate when describing the relation between suspended aerosol concentrations and stalagmite  $^{232}\text{Th}$  despite simplifications, that come with any interpolation model. Developing a customized interpolation model would require additional in-depth knowledge of local climate around individual cave sites throughout the Late Pleistocene. This was beyond the scope of this project, but could be applied to exemplary, individual records in future projects.

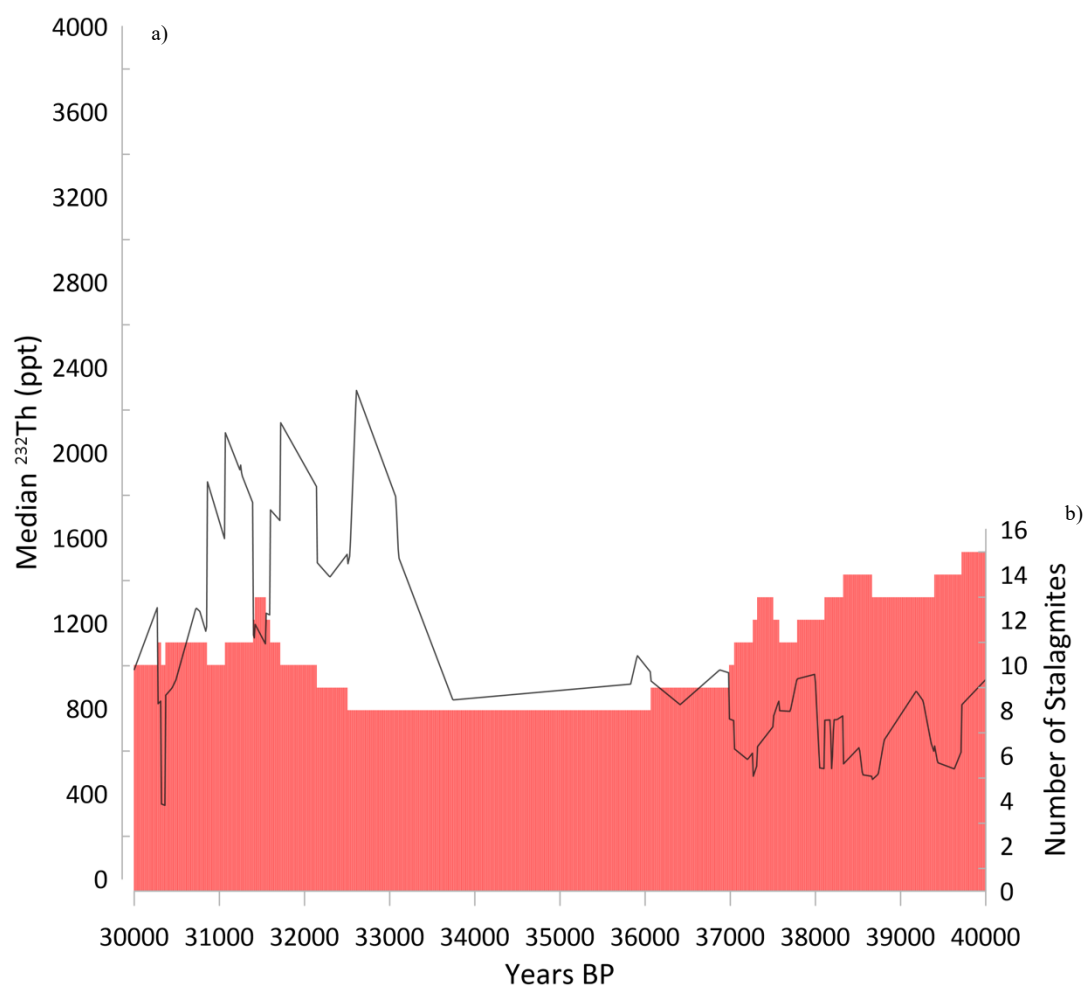


Figure 6, the black line illustrates the compiled median  $^{232}\text{Th}$  record between 40-30 ka. The red bar chart is a histogram of the number of records used to calculate each median value.

The choice of a linear interpolation model has resulted in sections of the compiled Asian  $^{232}\text{Th}$  curve exhibiting blocky and linear features. The period between 36060- and 32510- years BP (Figure 6a) illustrates an example of such a feature. This phenomenon is referred to as an interpolation gap throughout the remainder of this thesis. Interpolation gaps are caused by extended interruptions in measured  $^{232}\text{Th}$  concentrations that have been filled in by the interpolation model. In the above-mentioned example this occurs despite eight stalagmites contributing data during this window. These stalagmites include: XBL-3, TZ6, SO1, SJ1, SCO2, MSL, MSD and BAO2. This should be enough data to avoid interpolation gaps in the compiled curve. However, the stalagmites differ enough in  $^{232}\text{Th}$  concentrations throughout this period that the median value for any given decade between 36060- and 32510- years BP is always found within the same stalagmite record, resulting in the compiled median  $^{232}\text{Th}$  curve essentially recording a single interpolated stalagmite and producing an interpolation gap feature.

As discussed below, in section 4.2.3, interpolation gaps do present a limitation to this compilation methodology. Although compiling a mean instead of a median would decrease the severity of this issue, this triggers several other difficulties (as discussed above). In order to maximise the potential of  $^{232}\text{Th}$  as a proxy for dust flux, future research will require a solution to this statistical dilemma.

### 3.5 Comparison of a compiled $^{232}\text{Th}$ with a Loess Dust Flux Record

Reconstructing mineral dust flux patterns has been a key component to understanding past climates, especially regarding their role in glacial-interglacial cycles during the Last Glacial Period. Previous reconstruction methodologies include calculating mass accumulation rates (MAR) between dated soil horizons within loess-paleosol sequences. These sequences are often dated using radiocarbon or optical dating methods (including thermoluminescence, optically stimulated luminescence (OSL) and infrared OSL techniques). A combination of two

or more ages from these methods provides highly reliable age profiles. Where only one age can be produced amino acid racemization, magnetic susceptibility and/or pedostratigraphical evidence can also be used to correlate age profiles and boost the confidence in them (Újvári, 2010). However, these methods are subject to the errors and limitations of the dating methodologies used, including the extent of dateable age ranges. A comparison with the median  $^{232}\text{Th}$  curve highlights the accuracy of the thorium data as a dust flux proxy and the advantages of an absolutely  $^{234}\text{U}/^{230}\text{Th}$  dated dust flux proxy record (where the loess record becomes less reliable further back in the archived record).

Compiled  $^{232}\text{Th}$  data from Asian stalagmites is compared with a loess record dust flux reconstruction (Figure 5; Guo et al., 2009). Guo et al. calculate dust flux through the multiplication of  $\text{Fe}_2\text{O}_3$  content by sedimentation rate and the mean dust density (which is

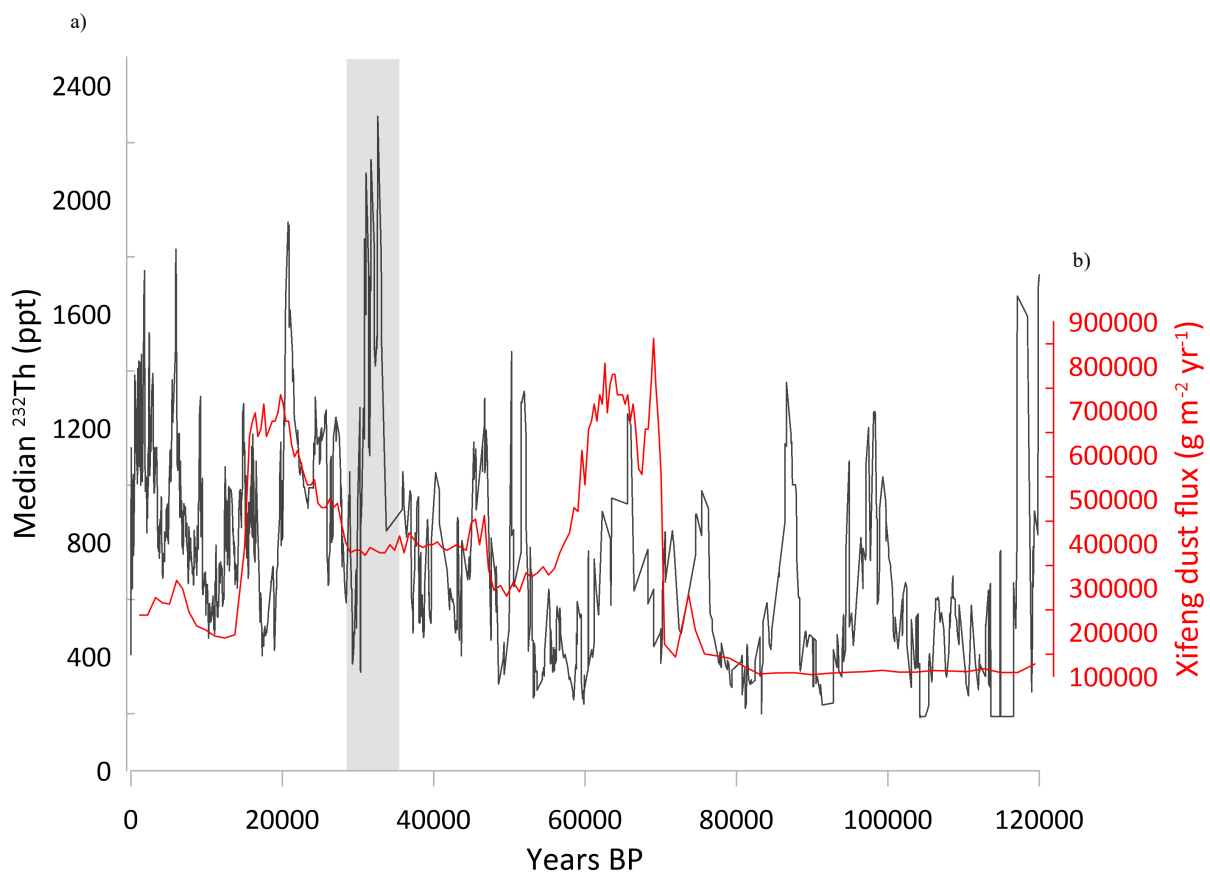


Figure 7a (black line) reconstructs paleo-aridity in EA between 120-0 ka, using median  $^{232}\text{Th}$  as a proxy for dust flux. Figure 7b (red line) is a paleo-aridity reconstruction for the same region and time period using a traditional loess record as a method for dust flux reconstruction.

assumed to be  $2.5\text{ g m}^{-3}$ ). Loess dust flux records produced from Xifeng, in northern China, have a mean temporal resolution of  $\sim 800$  years. This is an 80-times lower resolution than the  $^{232}\text{Th}$  curve presented in this study (Figure 7a).

A similar trend is observed in both curves during the last 80 ka, before which the Loess dust flux reconstruction has less variation. Differences between the two records include the duration and timing of the last glacial maximum (LGM). The loess record places the LGM at 18 ka, whereas the  $^{232}\text{Th}$  data records the LGM at 21 ka. Although both records display a gradual build up to the LGM, the loess reconstruction records an elongated peak (from 20-16 ka) whereas  $^{232}\text{Th}$  data on the other hand suggests a shorter, more abrupt, LGM. This could be due to individual cave sites being compiled and levelling out the build-up phase while emphasising the actual LGM periods.

Both records display similar first order trends. However, a noticeable difference is the 33kyr BP event recorded in the stalagmite  $^{232}\text{Th}$  curve, (grey bar in Figure 7). This peak in  $^{232}\text{Th}$  concentration, and therefore in atmospherically suspended dust aerosols, is not recorded in the loess record. The timing of this peak suggests that this could be representative of Heinrich Event 3. The impact of Heinrich and Dansgaard-Oeschger events on Asian dust flux are discussed in sections 4.2 and 4.3.

The largest discrepancy between the records occurs between 120-80 ka and demonstrates the potential advantage of using  $^{232}\text{Th}$  as a proxy for dust flux. During this interval the loess record is very stable and records only minor deviations from a  $100,000\text{ g m}^{-2}\text{ yr}^{-1}$  value. However, the  $^{232}\text{Th}$  curve contains three large peaks at 85, 100 and 120 ka, and two clear troughs at 90 and 105 ka. The shape of the trough at 118 ka suggests that the interval reflects inadequate data rather than climate trends. The lack of variation in dust flux recorded by the loess record after approximately 80 ka suggests that this loess record has lost its accuracy and no longer records variations in aerosol concentrations reliably. However, the absolute

dating associated with the speleothem data retains a high degree of dating certainty even during older time periods. Using stalagmite  $^{232}\text{Th}$  data could permit more accurate dust flux reconstructions than have been previously been available.



## 4.0 Discussion

Having established the methodology and applied  $^{232}\text{Th}$  as a proxy to reconstruct Asian dust flux in the previous section, a comparison of this proxy record with a global sea level record establishes that Asian  $^{232}\text{Th}$  is climate controlled (Figure 8). The Asian  $^{232}\text{Th}$  curve is then interpreted through a comparison with numerous  $\delta^{18}\text{O}$  records, illustrating its value of  $^{232}\text{Th}$  as a paleoclimate proxy (Figure 9).

### 4.1 Correlation with global ice volume

Siddall et al. (2003) analysed oxygen isotope records from sediment cores to reconstruct water residence times in the Red Sea. Using a hydraulic model of the water exchange between the Red Sea and the world's oceans Siddall et al. (2003) reconstruct global sea level with an accuracy of  $\pm 12\text{m}$  and a centennial-scale resolution from 70 to 25 ka (Figure

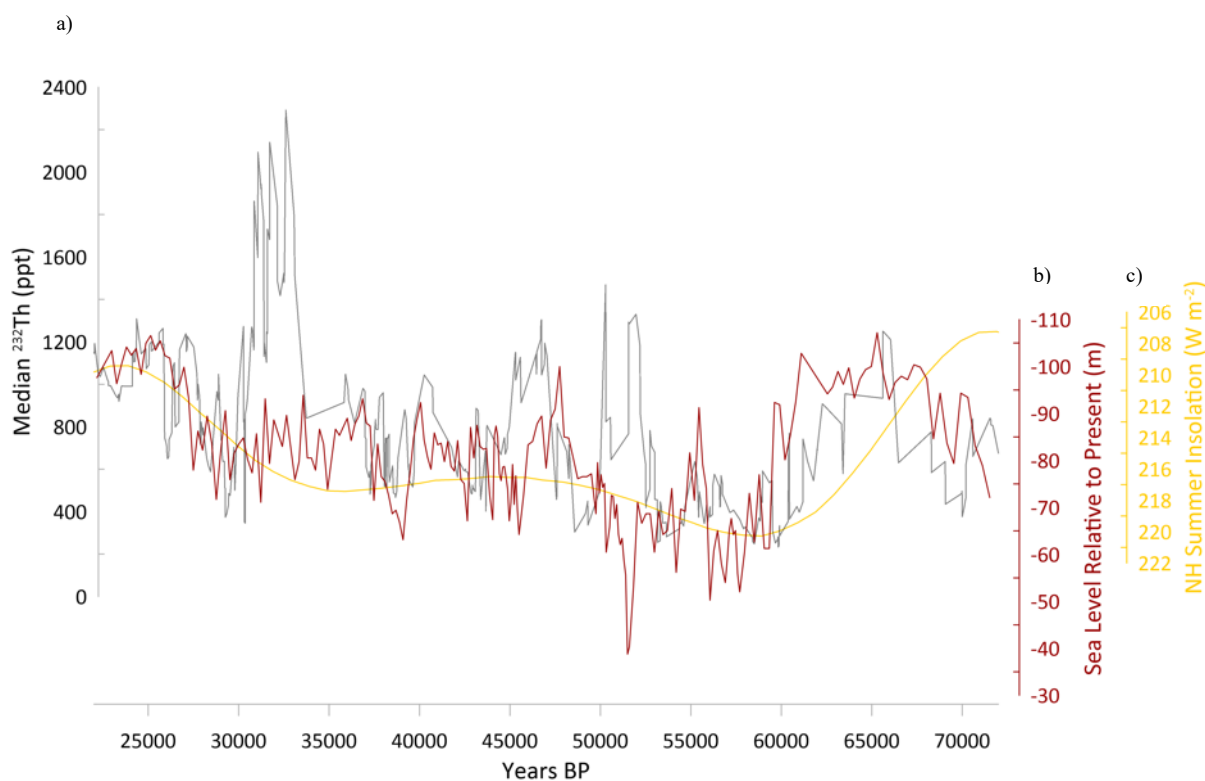


Figure 8a (grey) shows a compiled, Asian median  $^{232}\text{Th}$  curve. Figure 8b (red) is a curve representing Red Sea sea level relative to present day sea level, used as a proxy for global sea level. Figure 8c (yellow) is a NH ( $65^\circ$ ) summer insolation model (Berger and Loutre, 1991).

8b). These results were compared to a scaled plot of the high-resolution deep-sea  $\delta^{18}\text{O}$  record of eastern North Atlantic core MD952042 and displayed a high signal agreement. The only realistic influences on the deep-sea  $\delta^{18}\text{O}$  record of MD952042 are global ice volume (hence, sea level) and deep-sea temperature changes. Here, reconstructed Red Sea sea level is used as a proxy for global sea level and compared to compiled Asian stalagmite  $^{232}\text{Th}$  median concentration (Figure 8).

This comparison produces a positive correlation between 75-20 ka ( $r^2 = 0.32$ ,  $p < 0.00001$ ,  $n = 213$ ) (Figure 8). An overall decrease is observed in both curves between 60 and 20 ka, with intermittent peaks and troughs aligning. A curved, dome shaped feature, with a maximum at 65 ka, is visible between 75 and 60 ka in both records. This correlation is highlighted by the NH Summer Insolation model (Figure 8c), which matches the trends of both records.

Exceptions to this relationship are found at 33 and 52 ka. Interestingly, the peak in stalagmite  $^{232}\text{Th}$  at 33 ka is also discussed as an outlier below when EAM  $\delta^{18}\text{O}$  records are compared to median  $^{232}\text{Th}$  concentrations. At 52 ka the Red Sea sea level record exhibits a sudden rise in global sea level, which coincides with an increased Asian dust flux. A proposed explanation for this divergence is the coinciding occurrence of Dansgaard-Oeschger (D-O) event 14. The relation between Asian stalagmite  $^{232}\text{Th}$  and D-O events is discussed in further detail in later sections.

The correlation between global ice volume, the compiled  $^{232}\text{Th}$  curve and the superimposed NH insolation data suggests a teleconnection between global, regional and local climate. This connection between local dust flux proxies to large scale ice volume and NH temperature trends is explored in the following section.

#### 4.2 Analysis of correlation between $\delta^{18}\text{O}$ records and $^{232}\text{Th}$ concentrations

Figure 9 compares NH summer (July) insolation at  $65^\circ$  latitude (Berger and Loutre, 1991), NGRIP  $\delta^{18}\text{O}$  (data from: North Greenland Ice-Core Project Members, 2004), compiled EA stalagmite  $\delta^{18}\text{O}$  (referred to as EAM  $\delta^{18}\text{O}$  below) (data from: Cheng et al., 2016) and the interpolated  $^{232}\text{Th}$  data from Asian stalagmites. There is a clear correlation between the NH insolation model and both  $\delta^{18}\text{O}$  and  $^{232}\text{Th}$  curves (highlighted by superimposition of the insolation curve on figures 9a, b and c), suggesting that NH summer insolation is a dominant control on East Asian dust flux. This is explored further through the analysis of EAM  $\delta^{18}\text{O}$  and  $^{232}\text{Th}$  correlations, and an interval of weaker correlation between the two plots from 55 to 20 ka (Figure 9). An explanatory hypothesis for this interval is detailed in section 4.2.3.

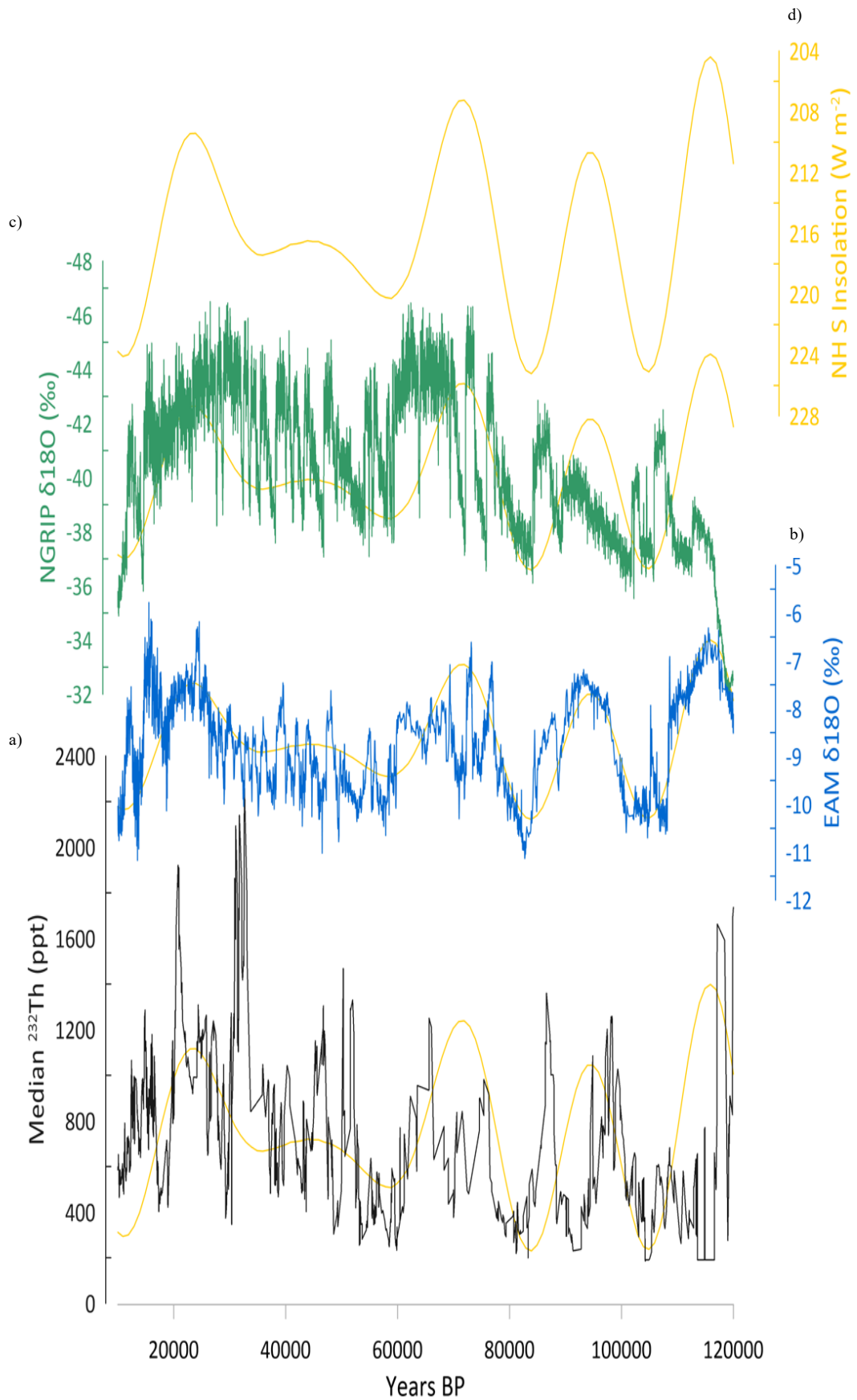


Figure 9a (black) shows a compiled Asian, median  $^{232}\text{Th}$  curve. Figure 9b (blue) is an EAM stalagmite  $\delta^{18}\text{O}$  record. Figure 9c (green) NGRIP  $\delta^{18}\text{O}$  record. Figure 9d (yellow) is a NH  $65^\circ$  summer insolation model, which is also superimposed on all other curves to highlight the degree of correlation.

#### 4.2.1 East Asian Monsoon Data

Two different time series are plotted, 20-10 and 90-50 ka, comparing compiled EAM  $\delta^{18}\text{O}$  and median  $^{232}\text{Th}$  values (Figure 10). These two intervals were selected because they highlight the correlation between the two records.

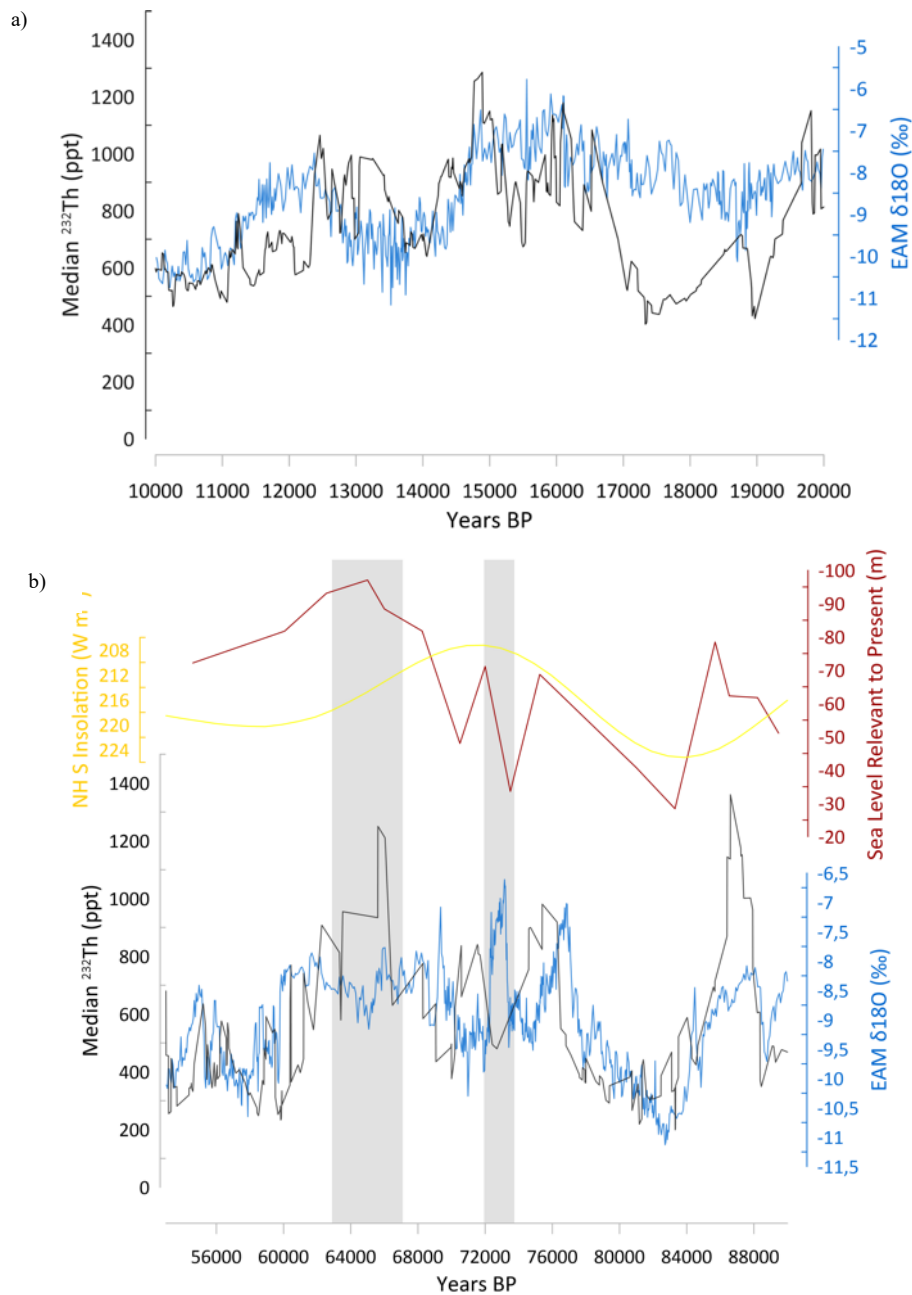


Figure 10a (top) shows a compiled Asian, median  $^{232}\text{Th}$  curve (black) plotted with a compiled stalagmite an EAM stalagmite  $\delta^{18}\text{O}$  record (blue) between 20-10 ka. Figure 10b (bottom) plots the same curves between 90-50 ka as well as a Red Sea sea level record (red), as a proxy for global sea level variation and a NH  $65^\circ$  summer insolation model (yellow).

Near the end of the Pleistocene, both curves peak at approximately 12,500 years BP (Figure 10a), followed by a drop and a rise back up, to elevated concentrations and reduced  $\delta^{18}\text{O}$  values respectively, which is sustained from 17-14 ka. The overall trend between these two plots correlates strongly ( $r^2=0.34$ ,  $p < 0.00001$ ,  $n = 807$ ) although the  $^{232}\text{Th}$  concentration does decrease more significantly at 17 ka before rising again.

The forty-thousand-year period between 90-50 ka highlights a remarkable correlation between the sea level and EA dust flux (EADF) (Figure 10b), and an additional link between insolation and Red Sea sea level suggests that the correlation between EAM  $\delta^{18}\text{O}$  and  $^{232}\text{Th}$  during this interval is climate controlled. Periods of low insolation and low global ice volume coincide with intervals of high EAM  $\delta^{18}\text{O}$  values and low  $^{232}\text{Th}$  concentrations (Figure 9). Peaks in  $^{232}\text{Th}$  concentration, and therefore dust flux, such as at 64 or 85 ka coincide with lower  $\delta^{18}\text{O}$  values (interpreted as lower volumes of precipitation) and with peaks in global ice volume and minimal NH summer insolation.

Tropical and subtropical monsoons respond dominantly and directly to changes in NH summer insolation (Wang et al., 2008). Beyond supporting the idea presented by Wang et al. (2008), the correlations described above also suggest that East Asian dust fluxes are dominantly controlled by insolation cycles through their effects on the intensity and geographical extent of the EAM. Larger temperature differences, and therefore energy differences, between the Asian Continent and Pacific Ocean, are often observed during peak insolation time intervals (i.e. interstadials), and result in the Intertropical Convergence Zone (ITCZ) being drawn further north (Bischoff and Schneider, 2016). The ITCZ encircles the globe and is the zone where the Northern and Southern hemisphere trade winds meet, forming a permanent low-pressure zone (Yan, 2005). As a consequence of the ITCZ being drawn further north, the Asian continent experiences a more intense and extensive EAM during interstadial periods. During stadial periods there is a reduced temperature gradient between the continent and the Pacific Ocean.

As a result, stadial periods are characterised by weaker monsoons, which are recorded as heavier  $\delta^{18}\text{O}$  values in speleothem records (Waliser, 1993). This is based on the standard interpretation of  $\delta^{18}\text{O}$  records found in East Asian stalagmites in which the  $\delta^{18}\text{O}$  signal recorded is primarily a reflection of the ‘amount effect’, in which lighter  $\delta^{18}\text{O}$  is associated with increased rainfall amount (i.e. monsoon intensity) (Rohling, 2009). However,  $\delta^{18}\text{O}$  interpretations are often complex, with numerous geochemical and geographical controls, and can vary from one study/region to another. For example, Lisiecki et al. (2005) interpreted benthic foraminifera  $\delta^{18}\text{O}$  as a proxy for ice volume and global temperature. For the purpose of this study, the EAM  $\delta^{18}\text{O}$  illustrated in Figure 10 is interpreted in the standard context of the EAM. Other factors that influence  $\delta^{18}\text{O}$  values, such as temperature and moisture source, are not ignored, but assumed to be overpowered by the dominant amount effect.

Grey bars highlight two intervals of divergence between the records. Bar one (at approximately 65 ka) highlights a linear and block shaped period in the  $^{232}\text{Th}$  curve. However, during this interval the overall trend in both curves still correlate. This is not the case at 72 ka, where the second grey bar highlights the omission of a potential D-O event in the  $^{232}\text{Th}$  curve – which is visible in the  $\delta^{18}\text{O}$  data. Both intervals are very similar to the interpolation gap feature at 33 ka, discussed in section 3.5. These problematic intervals within this 40kyr period highlight the current limitations of  $^{232}\text{Th}$  derived dust flux reconstructions but do not detract from the overall correlation or from the proposed hypothesis for this period; Asian dust flux was controlled by the location of the ITCZ and subsequent intensity of the EAM, which was in turn controlled by NH insolation variability. The hypothesised role played by NH summer insolation can be both confirmed and expanded through the comparison of  $^{232}\text{Th}$  concentrations with Greenland ice core  $\delta^{18}\text{O}$  records.

#### 4.2.2 NGRIP $\delta^{18}\text{O}$ Data

$\delta^{18}\text{O}$  records from Greenland ice cores have previously been interpreted to predominantly reflect air temperatures above Greenland, as opposed to the ‘amount effect’ that forms the standard interpretation of East Asian stalagmite  $\delta^{18}\text{O}$  records. The interpretation that ice core  $\delta^{18}\text{O}$  records primarily reflect air temperatures is supported by a number of studies, such as the study of nitrogen isotopes in trapped air bubbles within the ice by Burns et al. (2003). Due to this interpretation the NGRIP  $\delta^{18}\text{O}$  ‰ axis in Figure 11 has been inverted, relative to the  $\delta^{18}\text{O}$  ‰ axes used in section 4.2.1.

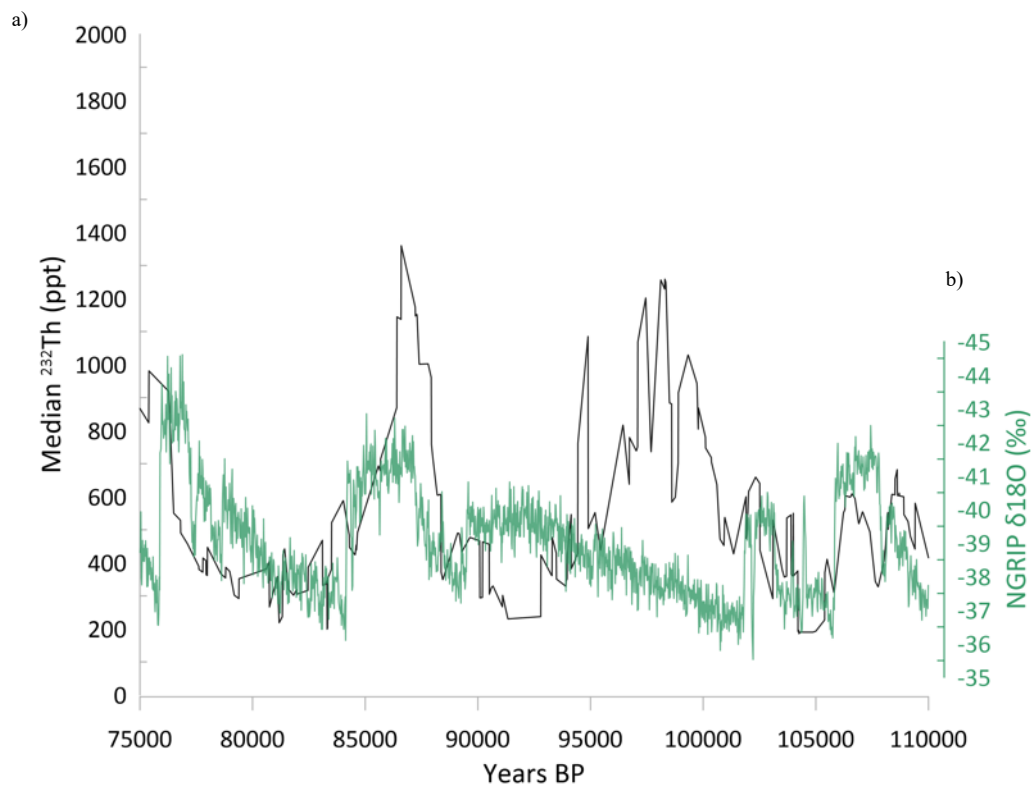


Figure 11a (black) shows a compiled Asian, median  $^{232}\text{Th}$  curve. Figure 11b (green) is the NGRIP ice core  $\delta^{18}\text{O}$  record.

Cooler NH temperatures are recorded as lower  $\delta^{18}\text{O}$  values, maxima are found at 107, 86 and 76 ka. Cooler NH temperatures lead to weaker heating differentials between continent and ocean surface waters, resulting in the ITCZ being drawn less far north and a weaker Asian monsoon (Waliser, 1993). This theory is supported by the alignment of NGRIP  $\delta^{18}\text{O}$  maxima



and peaks in median Asian  $^{232}\text{Th}$  (signifying colder, drier and dustier conditions) at 77, 87 and 107 ka.

The exception to the correlation described above is found in a 10kyr period between 100-90 ka. During this interval the  $^{232}\text{Th}$  curve shows 4 separate peaks, as opposed to a consistent decreasing trend in NGRIP  $\delta^{18}\text{O}$ . Eight to nine stalagmites contribute to the median curve during this 10kyr interval (Figure 6). Stalagmites KS06-A, KS06-1, KS06-2 and SX24, SX7 are from Kesang and Sanxing caves respectively and form over half of the records contributing to the curve during this interval. As a result, the local climates around these two caves impact the median  $^{232}\text{Th}$  curve (which is meant to represent regional dust flux) disproportionately compared to the other three or four stalagmites during this 10kyr period. It is therefore possible that these spikes could record local, singular events, rather than a regional climate trend that could be expected to match NGRIP  $\delta^{18}\text{O}$  data.

This correlation between compiled, Asian median  $^{232}\text{Th}$  data and the NGRIP  $\delta^{18}\text{O}$  record reinforces the conclusion drawn above (in sections 4.1 and 4.2), that NH insolation and temperature fluctuations control EAM intensity, and subsequent variation in Asian dust flux. This teleconnection has been highlighted at different intervals throughout the previous sections. The interval between 50 and 20 ka however has not been discussed, as it does not show the same significant correlation between  $^{232}\text{Th}$  data and regional (East Asian stalagmites) or hemispheric (NGRIP)  $\delta^{18}\text{O}$  records.

### 4.2.3 Problematic correlation period

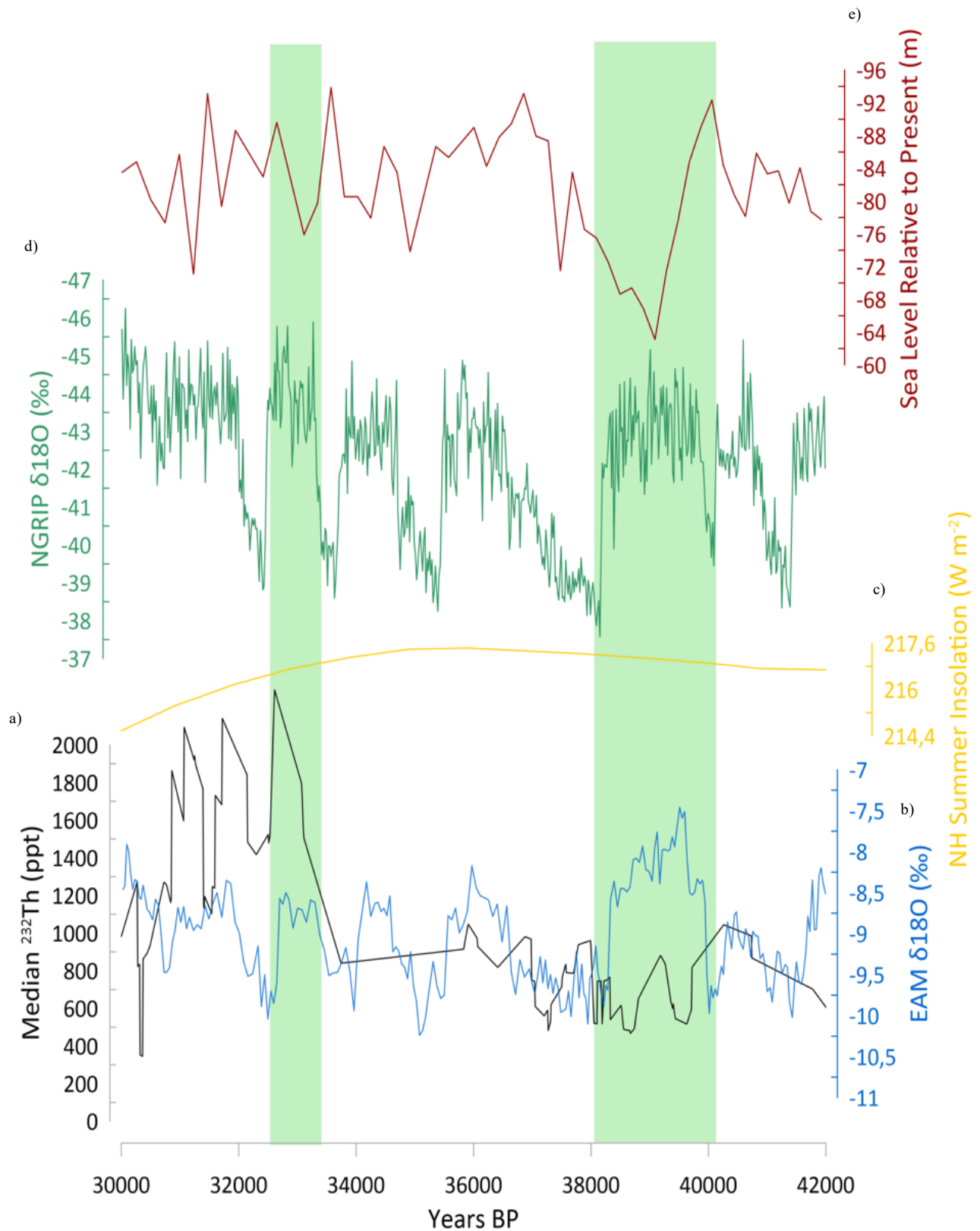


Figure 12a (black) shows a compiled Asian, median  $^{232}\text{Th}$  curve. Figure 12b (blue) is an EAM stalagmite  $\delta^{18}\text{O}$  record. Figure 12c (yellow) is a NH  $65^\circ$  summer insolation model. Figure 12d (green) is an NGRIP  $\delta^{18}\text{O}$  record. Figure 12e (red) is a Red Sea sea level record, used as a proxy for global sea level. Green bars highlight periods of correlation discussed below.

The intervals discussed above support the conclusion that differential heating of continental Asia and the Pacific Ocean, caused by NH summer insolation, is the primary control driving the EAM throughout the last glacial period. This is however not the case throughout the entire record.

Unlike the intervals discussed previously there is no clear correlation between EAM  $\delta^{18}\text{O}$  and median  $^{232}\text{Th}$  concentrations between 42-30 ka (Figure 12). That is not to say that there is none, areas of weaker correlation are highlighted by the green bars (Figure 12). The EAM  $\delta^{18}\text{O}$  is dominated by cyclic D-O events, identified by the comparison between the NGRIP and various stalagmite  $\delta^{18}\text{O}$  records in previous studies (Adolphi, 2018) and with the EAM  $\delta^{18}\text{O}$  record in Figure 12. The correlation between these peaks in the EAM  $\delta^{18}\text{O}$  and NGRIP  $\delta^{18}\text{O}$  might offer some evidence in the identification of these North Atlantic warming events. Some of these potential D-O events are also mirrored in the  $^{232}\text{Th}$  record. These include events at 32, 33, 36 and 39 ka. The D-O event recorded at approximately 34.5 ka in the EAM and NGRIP  $\delta^{18}\text{O}$  records does not appear in the  $^{232}\text{Th}$  curve, which is covered by an interpolation gap spanning a period of 3.55kyrs. Although these events establish that the overall trends of the  $^{232}\text{Th}$  and EAM  $\delta^{18}\text{O}$  curves are shared, the inconsistency of the amplitude of the identified D-O events suggest additional complexities.

This time period overlaps with a period of very little insolation variability (Figure 12c), and relatively little sea level change (when comparing Figure 12d to Figure 8). The lack of correlation between the NH insolation model, global sea level and the EAM  $\delta^{18}\text{O}$  record suggests that the previously presented mechanism driving EAM intensity (differential heating of the Asian continent and Pacific Ocean caused by variations in NH insolation) cannot explain the EAM  $\delta^{18}\text{O}$  record between 42-30 ka.

D-O and Heinrich events affect the Indian Summer Monsoon (ISM) and the Indian Ocean surface temperature (IOST) (Pausata et al. 2011). This conclusion is supported by Burns

et al. (2003) who found that the gradual cooling and sudden warming associated with D-O events, and visible in the NGRIP  $\delta^{18}\text{O}$  record (Figure 12d), correlate with the M1-2  $\delta^{18}\text{O}$  record. Stalagmite M1-2 was collected from Moomi cave on the eastern side of Socotra Island in the Indian Ocean. Burns et al. (2003), observing 8-year spaced isotopic measurements, found that the transition from drier to wetter conditions on Socotra Island took place across approximately 25 years, and occurred synchronously with NH temperature changes. Similarly, to the EAM, the ISM is driven by the temperature gradient between central Asia and the Indian Ocean. Modern records have shown that high ISM precipitation is often preceded by warm European winters and high Tibetan snow cover (Robock et al., 2003). A warm European winter leads to increased warming of central Asia and a larger land-sea thermal contrast (Burns et al., 2003). A similar teleconnection is suggested to link North Atlantic D-O events with the Indian Ocean climate recorded in M1-2.

In 2019, Guo et al. comprehensively investigated the moisture sources for Asian precipitation. Moisture sources were tracked using the Water Accounting Model-2layers (WAM-2layers) in 5 sub regions of East Asia. These regions were: the Tibetan Plateau, southeast, central east, northwest and northeast Asia. Guo et al. found that the annual mean moisture contributions for southeast Asia are: 16% is sourced locally, 30% from the Eurasian Continent, 37% from the Indian Ocean and 17% from the Pacific Ocean. These contributions vary with latitude. The Indian Ocean's contribution decreases from west to east across SEA, while the contributions from the Pacific Ocean decrease from east to west (Guo et al., 2019).

Based on these studies it can be considered that North Atlantic climate events possibly influence Indian Ocean conditions, including sea surface temperature and that variations in sea surface temperature could influence the  $\delta^{18}\text{O}$  signature of the water that is sourced from the Indian Ocean. Because the EAM sources 37% of its moisture from the Indian Ocean, changes in IOST are may be reflected in Chinese stalagmite  $\delta^{18}\text{O}$  records (Figure 12b). This contradicts

the standard interpretation of  $\delta^{18}\text{O}$  records from East Asian stalagmites, which are normally interpreted to reflect the ‘amount effect’. Elevated  $\delta^{18}\text{O}$  values indicate higher volumes of precipitation, rather than variations in  $\delta^{18}\text{O}$  signal from the moisture source. However, during a period of limited NH insolation variability EAM intensity remains consistent and stalagmite  $\delta^{18}\text{O}$  is able to record moisture source variations instead of differences in monsoon intensity.

This period of low NH insolation fluctuation, between 55-20 ka, coincides with the occurrence of 14 of the 20 D-O events and 4 of the 6 Heinrich Events (Figure 13).

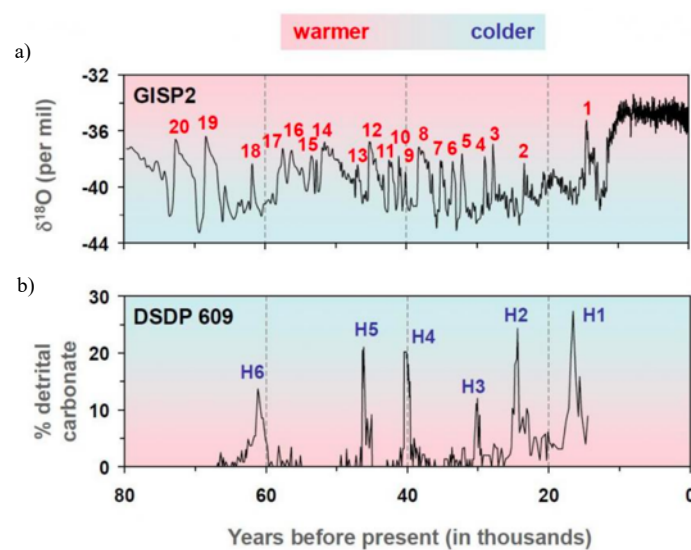


Figure 13a (top) is a  $\delta^{18}\text{O}$  record from the GISP2 ice core in Greenland, showing 20 of the 25 observed D–O events during the last glacial period (Grootes et al., 1993). Figure 13b (bottom) is a record of ice-rafted material during Heinrich events from a deep-sea core in the North Atlantic (Bond and Lotti, 1995). Taken from the NOAA website.

As discussed previously, NH summer insolation is the driving force behind the EAM and ISM. A lack of variability in insolation results in a steady intensity of the EAM between 42 and 30 ka. As a result, there are no large-scale changes in East Asian precipitation intensity. The stalagmite  $^{232}\text{Th}$  continues to record small scale, local variability in dust flux but no larger scale climate changes are observed. The stalagmite  $\delta^{18}\text{O}$  record however does show cyclic oscillations potentially corresponding to D-O events. This is could be explained by the stalagmite  $\delta^{18}\text{O}$  variations no longer solely being controlled by the ‘amount effect’, because precipitation volume is steady, but instead the oscillating signal reflects changes in the moisture

source, the Indian Ocean,  $\delta^{18}\text{O}$  signature. This would explain why during periods of low insolation variability the median  $^{232}\text{Th}$  and EAM  $\delta^{18}\text{O}$  curves do not correlate well; because they record different things.

In support of this hypothesis, it can be noted that outside of the 55-20 ka time interval similar features and patterns can be observed around the suggested timing of D-O events 19 and 20. During an interval of positive correlation, 90-55 ka, the two examples of decoupling between the  $\delta^{18}\text{O}$  and  $^{232}\text{Th}$  curves, at 69 and 73 ka, coincide with the timing of these 1 hypothesized D-O events (highlighted by the grey bars in Figure 14). This may suggest that when these North Atlantic events occurred, the EAM  $\delta^{18}\text{O}$  record records the shifts in IOST, whereas stalagmite  $^{232}\text{Th}$  continues to record local dust flux.

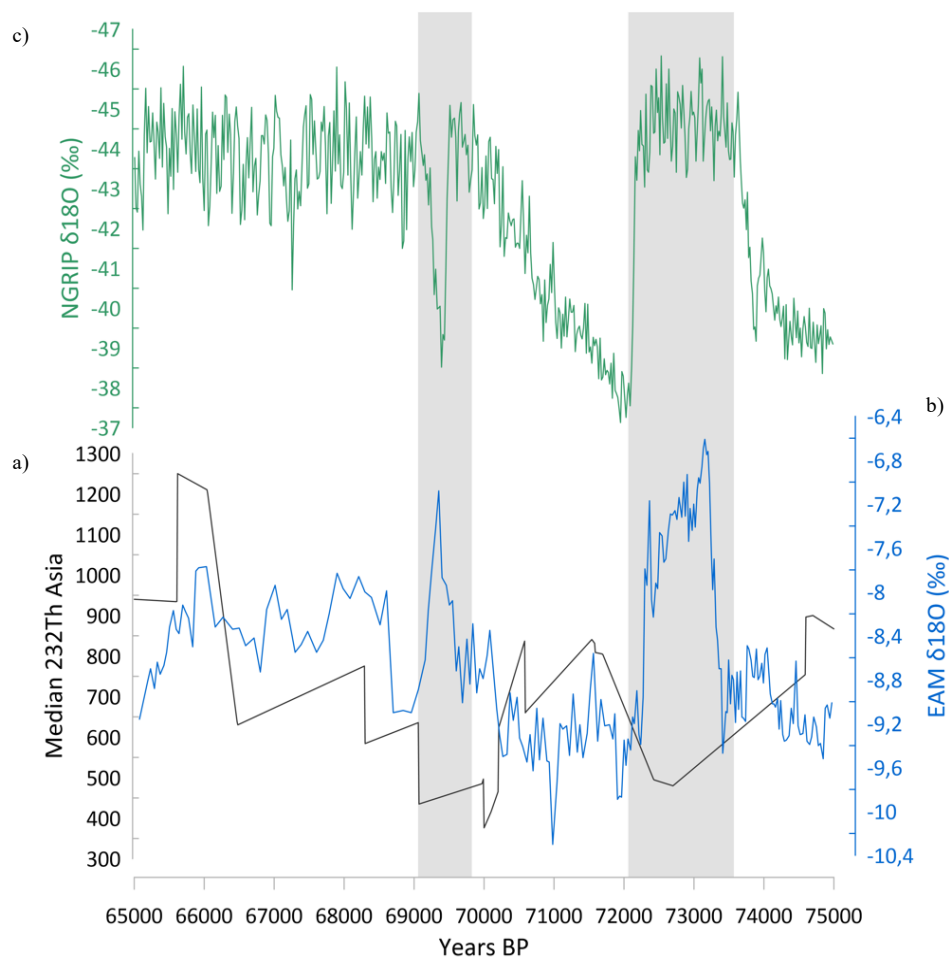


Figure 14a shows a compiled Asian, median  $^{232}\text{Th}$  curve (black). Figure 14b illustrates a compiled stalagmite an EAM stalagmite  $\delta^{18}\text{O}$  record (blue). Figure 14c (green) is the NGRIP ice core  $\delta^{18}\text{O}$  record.

As established previously the EAM sources 37% of its moisture from the Indian Ocean and 30% from the Eurasian continent (Guo et al., 2019). Guo et al. (2019) also showed that the primary moisture source for the seasonal mean differs from the annual mean for central-eastern, northwestern, and northeastern Asia. This is not the case over southeastern Asia and the Tibetan Plateau where the primary contributor does not change for the seasonal and annual means. For the mid-latitude regions mentioned above, extratropical sea contributions overtake extratropical land contributions as the primary contributor during winter months. This increased moisture comes from inland bodies of water such as the Mediterranean and Caspian Seas (Guo et al., 2019). Increased moisture sourcing from European and central Asian inland bodies of water helps explain why high ISM precipitation volumes are preceded by warm European winters. The Westerlies, which are strongest during the winter period, play an important role in transporting moisture from these inland bodies of water to the Asian Monsoon systems.  $\delta^{18}\text{O}$  records for Westerlies driven precipitation are therefore critical in establishing the teleconnection between NA climate, AM intensity and EADF.

#### 4.3 Westerlies $\delta^{18}\text{O}$ data

The Westerlies are the prevailing winds in the middle latitudes of the Earth's atmosphere and track from west to east between high-pressure areas above the tropics and low-pressure areas above the poles (Toggweiler, 2009). The position of the Westerlies responds to variations in the mean global temperature and gradients between the poles and ITCZ. At the peak of the LGM the southern-hemisphere Westerlies migrated so far northwards they were no longer aligned with the Atlantic Circumpolar Current (ACC). Over the past 50 years the Westerlies have strengthened and shifted poleward as a response to the global warming trend (Toggweiler, 2009). A comparison between  $\delta^{18}\text{O}$  associated with the Westerlies with the

compiled median  $^{232}\text{Th}$  (Figure 13) is valuable when trying to establish the Westerlies' role as a mediator within the teleconnection between NA climate and Asian monsoon systems.

Cheng et al. (2016) used  $\delta^{18}\text{O}$  records from both the Ton and Kesang caves, located in Uzbekistan and north-western China respectively, as a proxy for Westerlies driven precipitation (Figures 15b and 15c). Noticeably, the overall trend, of both  $\delta^{18}\text{O}$  records, correlates well with the  $^{232}\text{Th}$  curve ( $r^2=0.02$ ,  $p < 0.00001$ ,  $n=5000$  and  $r^2=0.04$ ,  $p < 0.00001$ ,  $n=5000$  for Ton and Kesang records respectively). This supports the discussion of the EAM  $\delta^{18}\text{O}$  record in section 4.2.3 and indicates that increased moisture flux from the Eurasian

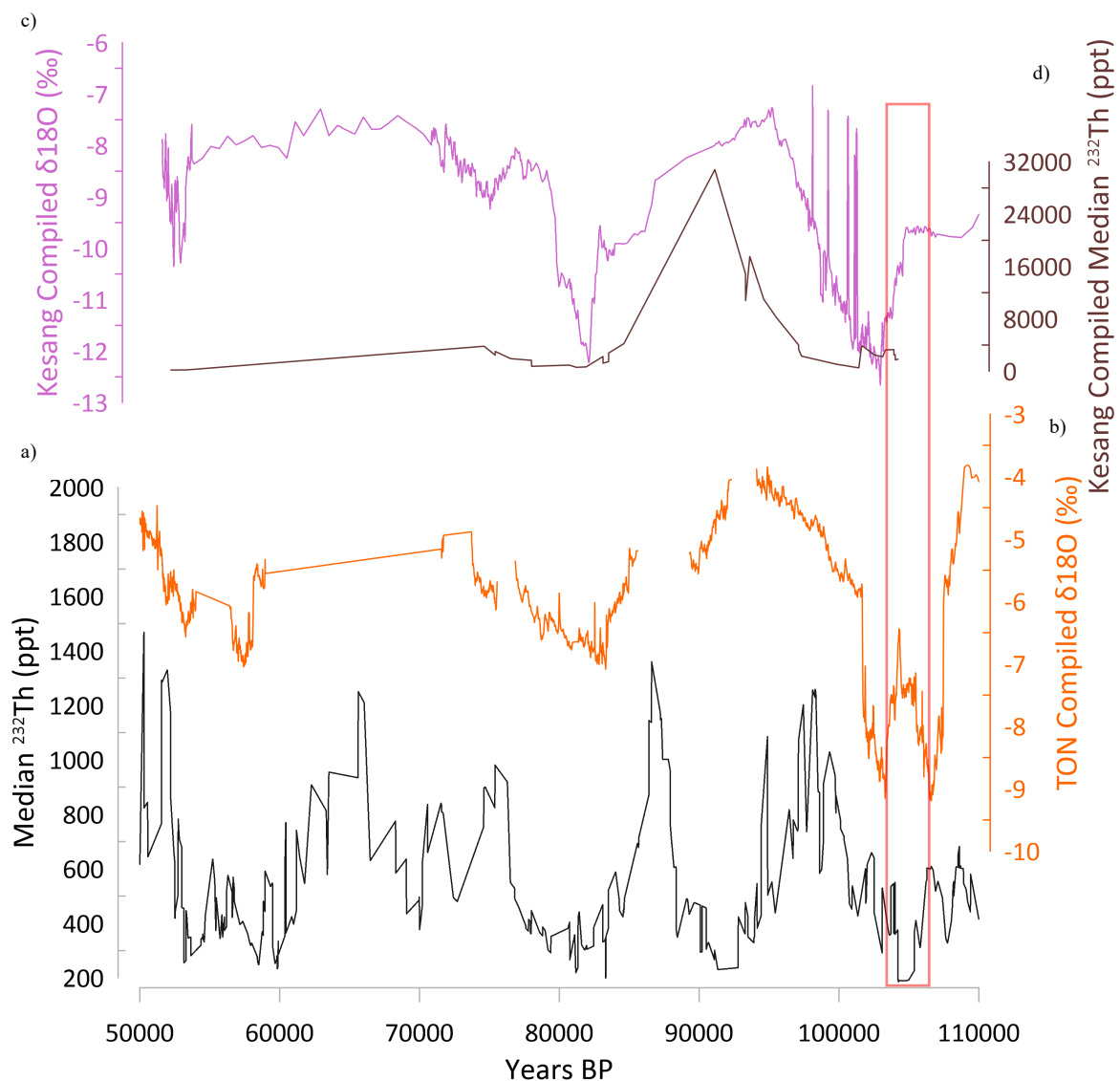


Figure 15a (black) illustrates a compiled Asian, median  $^{232}\text{Th}$  curve. Figure 15b (orange) is a TON compiled  $\delta^{18}\text{O}$  record. Figure 15c (violet) illustrates a Kesang cave compiled  $\delta^{18}\text{O}$  record. Figure 15d (brown) is a compiled, median  $^{232}\text{Th}$  curve from 5 stalagmites harvested in Kesang Cave.



continent could lead to increased EAM intensity and decreases stalagmite  $^{232}\text{Th}$  concentrations. This is supported by the correlation between Kesang Cave  $^{232}\text{Th}$  and  $\delta^{18}\text{O}$  records ( $r^2=0.17$ ,  $p < 0.00001$ ,  $n = 2423$ ) (Figure 15d).

This correlation continues until approximately 103 ka. During the time interval highlighted by the red rectangle (Figure 15), coinciding with the hypothesized Heinrich Event 10, the  $\delta^{18}\text{O}$  records behave oppositely to the  $^{232}\text{Th}$  curve. This figure therefore supports the suggestion made above that during a Heinrich Event the  $^{232}\text{Th}$  continues to record local aerosol concentrations and does not correlate with other moisture sources that contribute to the Asian monsoon.

Unfortunately, there is insufficient data recorded in the TON and Kesang stalagmites during the 42-30 ka interval to expand on the effects of D-O and Heinrich events on Westerlies  $\delta^{18}\text{O}$  records (Appendix 7). This could be explained by glaciation reaching its maximum extent in the Himalayan and Tibetan plateau region between 47 and 27 ka (Owen et al., 2002) and as a consequence inhibiting stalagmite growth from recording climate signals.

## 5.0 Conclusion

The correlation between recent stalagmite  $^{232}\text{Th}$  concentrations and the mean DCMD measured around each cave site, establishes the use of stalagmite  $^{232}\text{Th}$  concentrations as a proxy for atmospherically suspended dust flux. This correlation is demonstrated by an  $R^2$  value of 0.67 and a spearman's rank coefficient of 0.37. This conclusion allows for the utilization of the already existing, vast database of absolutely dated stalagmite  $^{232}\text{Th}$  aliquots to reconstruct global or regional paleo-dust fluxes up to 500 ka.

The Asian monsoon transfers heat and moisture across the Indian and Eastern Pacific Ocean into the Indian subcontinent and southeastern Asian continent (Cheng et al., 2016). Due to East Asia's dense population and socioeconomic importance, the EAM is an incredibly important climate system to understand when navigating future climate change.

This study compiled  $^{232}\text{Th}$  data from 194 Asian stalagmites found in 83 caves. Dated aliquots with age gaps smaller than 5,000 years were linearly interpolated across on a decadal resolution to produce a continuous Asian  $^{232}\text{Th}$  curve. This curve is based on median values from all relevant compiled stalagmites. The median is used instead of the mean to negate the impact of singular events, such as flooding or dust storms.

The compiled  $^{232}\text{Th}$  curve is compared to a compiled  $\delta^{18}\text{O}$  curve from different Chinese stalagmites, produced by Cheng et al. in 2016. East Asian stalagmite  $\delta^{18}\text{O}$  has previously been interpreted as a reflection of the EAM intensity. The  $\delta^{18}\text{O}$  record is reflective of the 'amount affect' by which high intensity monsoon intervals are recorded as more negative  $\delta^{18}\text{O}$  values. This interpretation aligns well with the  $^{232}\text{Th}$  data between 20-10 and 90-50 ka. The EAM  $\delta^{18}\text{O}$  record and median  $^{232}\text{Th}$  curve correlate during these intervals ( $r^2=0.17$ ,  $p < 0.00001$ ,  $n = 1001$  and  $r^2 = 0.01$ ,  $p < 0.00001$ ,  $n = 3401$ ) (Figures 10a and 10b). This suggests that the Asian monsoon system acts as one of the controlling factors on Asian dust flux. NH summer insolation (July,  $65^\circ$  latitude) acts as a first order control on both the  $^{232}\text{Th}$  and  $\delta^{18}\text{O}$  curves

(Figure 9c). Periods with high insolation lead to a larger disparity in heating between the Pacific Ocean and continental Asia; resulting in more intense monsoon seasons. The opposite is true for intervals of lower insolation.

The interval between 45-20 ka is characterized by little to no variation in NH insolation. Based on the first order control established above this should promote a stable EAM intensity, however the EAM  $\delta^{18}\text{O}$  record is characterized by, what have cautiously been identified as, cyclic D-O events, which do not appear in the  $^{232}\text{Th}$  record. This can potentially be explained by the teleconnection between IOST and North Atlantic D-O and Heinrich Events. This paper presents the hypothesis that increased IOST result in an increased  $\delta^{18}\text{O}$  signal. Because the EAM sources 37% of its moisture from the Indian Ocean this change is recorded in the monsoonal  $\delta^{18}\text{O}$  signal. The cyclic pattern, characterizing East Asian stalagmite  $\delta^{18}\text{O}$  records during this time interval, does therefore not reflect monsoon intensity, based on the amount effect, but instead reflects changes in source moisture  $\delta^{18}\text{O}$  values. Meanwhile, the monsoon intensity shows little variation due to steady NH insolation.  $^{232}\text{Th}$  continues to record local dust flux and as a result decouples from the signal recorded in the stalagmite  $\delta^{18}\text{O}$  record during this interval. Understanding the functions of these teleconnections during the late Pleistocene will help to predict future AM fluctuations/variability in response to changing NH and global climate.

This study has shown that  $^{232}\text{Th}$  is a reliable proxy record for dust flux in East Asia during the late Pleistocene. However, it has also highlighted limitations associated with this method as currently developed, centered around data availability and statistical methodology. Valuable extensions to this study would include increasing data availability from arid regions around the globe (e.g., in chapter 2.1 the gap in high  $^{232}\text{Th}$  concentrated stalagmite aliquots is described). Increased sampling from regions such as northern Africa and central Australia might fill this gap and help complete the record. A larger sample of high  $^{232}\text{Th}$  aliquots would

help improve the robustness of the observed correlation. Additionally, increased recording of  $^{232}\text{Th}$  concentrations in laminae that are considered “too dirty” to date, could increase the availability of high  $^{232}\text{Th}$  concentration aliquots. Furthermore, the level of scrutiny applied to stalagmites disqualified from the correlation curve can be reviewed further and applied to all available stalagmites to produce more robust dust flux reconstructions.

We note that  $^{232}\text{Th}$  data is not necessarily restricted to U-Th dates but is also easily and quickly produced via laser ablation mass spectrometry, and these copious new data could supplement existing datasets. These modifications would contribute to producing a more robust correlation curve and strengthen the relationship discussed in Chapter 2 between DCMD and recent  $^{232}\text{Th}$  concentrations.

An exponential decline in data availability with time is highlighted in Figure 6b. Lack of data past the upper Pleistocene hinders the production of a reliable  $^{232}\text{Th}$  curve. Accurate dating up to 500 ka is one of the main benefits to the methodology of using  $^{232}\text{Th}$  as a proxy for dust. In order to maximize the potential, more data needs to be collected from older stalagmite laminae, thus extending the  $^{232}\text{Th}$  proxy record further.

Moreover, data from a reliable stalagmite with recent, annual growth laminae could be used to calibrate  $^{232}\text{Th}$  concentrations and modern DCMD data throughout recent decades. This would produce a higher resolution, recent proxy record, that could be calibrated against, potentially, annual dust flux patterns. An investigation into the transport, across the Atlantic, and deposition of Saharan sourced aerosol particles in the Caribbean is an excellent example of a potential extension of this project that would utilize high quality, and resolution, stalagmite data in investigating another climate teleconnection.

Figure 7 draws attention to the interpolation gap phenomena seen repeatedly throughout the median  $^{232}\text{Th}$  curve produced for this study, caused by the utilization of the median instead of the mean. The difference in  $^{232}\text{Th}$  concentrations between stalagmites means that within a

selection of stalagmites the median value will always be found in the same stalagmite. As a result, the curve records the linear interpolation between data points from one stalagmite rather than compiling data from all of the stalagmites available for a given time interval. This could be improved with increased data availability, as seen by the reduced occurrence of the interpolation gap within the Holocene record, or by a more sophisticated statistical approach, such as the calculation of a mean value after the removal of statistical outliers. Future studies could examine the interpolation method applied in the production of a median  $^{232}\text{Th}$  curve. While this study applies a linear interpolation model on a decadal time scale, future studies could take advantage of new data availability and knowledge to experiment with variations of interpolation models and time resolutions. These novel approaches may be more appropriate on various time resolutions or even throughout different geographical regions or periods of time. This study maintained a very simple, broad-brush approach and has left a lot of room for future model finetuning and optimization.

Increased modern  $^{233}\text{Th}$  data could highlight a more appropriate correlation shape than the linear line of best fit found in this study (figure 2). An improved understanding of the correlation between modern DCMD and  $^{232}\text{Th}$  concentrations in stalagmite aliquots could lead to the discovery of more appropriate data modelling methods to produce an interpolated dust flux proxy record, as mentioned above. Potentially variations in growing conditions and cave geometries could be considered and the transport of dust within a cave could be investigated through the effect it has on  $^{232}\text{Th}$  concentrations in stalagmite aliquots. This study ignored factors such as distance to cave entrance, number of cave entrances, cave ventilation, passage and chamber heights and diameters, etc. All of which would be valuable to explore regarding their impact of dust deposition on growing stalagmites.

This study has compiled 435 stalagmites with a global distribution (Figure 1). However, its focus has been on the EAM and Asian dust flux. Utilizing this methodology in other regions

of the globe and viewing it within the context of other proxy records, would prove useful to further develop and understand the use of  $^{232}\text{Th}$  as a dust flux proxy, as well as providing additional insight into other climate systems around the globe.

In conclusion, this study has tested stalagmite  $^{232}\text{Th}$  concentrations as a proxy for atmospheric dust flux and found that this technique is viable. Uranium/thorium dating of stalagmite carbonate permits a more robust chronology than available for most dust flux archives, and the wide availability of thorium data permits the construction of decadal-resolved records which are an improvement on previous dust flux proxy records. This thesis has established the use of stalagmite thorium concentrations as an exciting new dust flux proxy to supplement existing archives.

## References

Please see the additional Excel sheet (Verniers000832400-References) for references of the 435 compiled stalagmite data set. References relevant to the written thesis are listed below.

Akers, P.D., Brook, G.A., Railsback, L.B., Liang, F., Iannone, G., Webster, J.W., Reeder, P.P., Cheng, H. and Edwards, R.L., 2016. An extended and higher-resolution record of climate and land use from stalagmite MC01 from Macal Chasm, Belize, revealing connections between major dry events, overall climate variability, and Maya sociopolitical changes. *Palaeogeography, Palaeoclimatology, Palaeoecology*, 459, pp.268-288.

Albani, S., Balkanski, Y., Mahowald, N. *et al.* Aerosol-Climate Interactions During the Last Glacial Maximum. *Curr Clim Change Rep* 4, 99–114 (2018). <https://doi.org/10.1007/s40641-018-0100-7>

Allen, B., 2017. *Atmospheric Aerosols: What Are They, And Why Are They So Important?*. [online] NASA. Available at: <https://www.nasa.gov/centers/langley/news/factsheets/Aerosols.html> [Accessed 25 April 2020].

An, ZhiSheng, et al. "Late Quaternary dust flow on the Chinese loess plateau." *Catena* 18.2 (1991): 125-132.

Andersen, Katrine K., et al. "High-resolution record of the Northern Hemisphere climate extending into the last interglacial period." *Nature* 431 (2004): 147-151.

Asmerom, Y., Polyak, V., Burns, S. and Rasmussen, J., 2007. Solar forcing of Holocene climate: New insights from a speleothem record, southwestern United States. *Geology*, 35(1), pp.1-4.

Arcgis.com. 2020. *What Are Proxy Records*. [online] Available at: <https://www.arcgis.com/apps/MapJournal/index.html?appid=1304b98bcb4f4ad2bca0e87db678513d> [Accessed 2 September 2020].

Brahim, Y.A., Cheng, H., Sifeddine, A., Wassenburg, J.A., Cruz, F.W., Khodri, M., Sha, L., Pérez-Zanón, N., Beraaouz, E.H., Apaéstegui, J. and Guyot, J.L., 2017. Speleothem records decadal to multidecadal hydroclimate variations in southwestern Morocco during the last millennium. *Earth and Planetary Science Letters*, 476, pp.1-10.

Berger, A., and Loutre, M. F., 1991. Insolation values for the climate of the last 10 million years. *Quaternary Science Reviews*, 10(4), 297-317.

Bischoff, T. and Schneider, T., 2016. The equatorial energy balance, ITCZ position, and double-ITCZ bifurcations. *Journal of Climate*, 29(8), pp.2997-3013.

Borsato, A., Frisia, S. and Miorandi, R., 2015. Carbon dioxide concentration in temperate climate caves and parent soils over an altitudinal gradient and its influence on speleothem growth and fabrics. *Earth Surface Processes and Landforms*, 40(9), pp.1158-1170.

Burns, S.J., Fleitmann, D., Matter, A., Kramers, J. and Al-Subbary, A.A., 2003. Indian Ocean climate and an absolute chronology over Dansgaard/Oeschger events 9 to 13. *Science*, 301(5638), pp.1365-1367.

Burns, S.J., Godfrey, L.R., Faina, P., McGee, D., Hardt, B., Ranivoharimanana, L. and Randrianasy, J., 2016. Rapid human-induced landscape transformation in Madagascar at the end of the first millennium of the Common Era. *Quaternary Science Reviews*, 134, pp.92-99.

Cheng, H., Edwards, R.L., Sinha, A., Spötl, C., Yi, L., Chen, S., Kelly, M., Kathayat, G., Wang, X., Li, X. and Kong, X., 2016. The Asian monsoon over the past 640,000 years and ice age terminations. *nature*, 534(7609), pp.640-646.

Cheng, H., Spötl, C., Breitenbach, S.F., Sinha, A., Wassenburg, J.A., Jochum, K.P., Scholz, D., Li, X., Yi, L., Peng, Y. and Lv, Y., 2016. Climate variations of Central Asia on orbital to millennial timescales. *Scientific Reports*, 6, p.36975.

Chen, S., Jiang, N., Huang, J., Xu, X., Zhang, H., Zang, Z., Huang, K., Xu, X., Wei, Y., Guan, X. and Zhang, X., 2018. Quantifying contributions of natural and anthropogenic dust emission from different climatic regions. *Atmospheric Environment*, 191, pp.94-104.

Chen, S., Hoffmann, S.S., Lund, D.C., Cobb, K.M., Emile-Geay, J. and Adkins, J.F., 2016. A high-resolution speleothem record of western equatorial Pacific rainfall: Implications for Holocene ENSO evolution. *Earth and Planetary Science Letters*, 442, pp.61-71.

Cosford, J., Qing, H., Eglington, B., Matthey, D., Yuan, D., Zhang, M. and Cheng, H., 2008. East Asian monsoon variability since the Mid-Holocene recorded in a high-resolution, absolute-dated aragonite speleothem from eastern China. *Earth and Planetary Science Letters*, 275(3-4), pp.296-307.

Duan, W., Kotlia, B.S. and Tan, M., 2013. Mineral composition and structure of the stalagmite laminae from Chulerasim cave, Indian Himalaya, and the significance for palaeoclimatic reconstruction. *Quaternary International*, 298, pp.93-97.

Dorale J.A., Edwards R.L., Alexander E.C., Shen CC., Richards D.A., Cheng H. (2004) Uranium-Series Dating of Speleothems: Current Techniques, Limits, & Applications. In: Sasowsky I.D., Mylroie J. (eds) Studies of Cave Sediments. Springer, Boston, MA

FAO, 2018. *World Food And Agriculture Statistical Pocketbook*. FAO Statistics. [online] Rome: Food and Agriculture Organization of the United Nations. Available at: <<http://www.fao.org/3/CA1796EN/ca1796en.pdf>> [Accessed 14 August 2020].

Fleitmann, D., Burns, S.J., Neff, U., Mudelsee, M., Mangini, A. and Matter, A., 2004. Palaeoclimatic interpretation of high-resolution oxygen isotope profiles derived from annually laminated speleothems from Southern Oman. *Quaternary Science Reviews*, 23(7-8), pp.935-945.

Global Modeling and Assimilation Office (GMAO) (2015), MERRA-2 tavgM\_2d\_aer\_Nx: 2d,Monthly mean,Time-averaged,Single-Level,Assimilation,Aerosol Diagnostics V5.12.4,



Greenbelt, MD, USA, Goddard Earth Sciences Data and Information Services Center (GES DISC), Accessed: [22/05/2020]

Frisia, S., 2019. Stalactites and stalagmites. In *Encyclopedia of Caves* (pp. 1041-1048). Academic Press.

Guo, L., van der Ent, R.J., Klingaman, N.P., Demory, M.E., Vidale, P.L., Turner, A.G., Stephan, C.C. and Chevuturi, A., 2019. Moisture sources for East Asian precipitation: Mean seasonal cycle and interannual variability. *Journal of Hydrometeorology*, 20(4), pp.657-672.

Guo, Z.T., Berger, A., Yin, Q.Z. and Qin, L., 2009. Strong asymmetry of hemispheric climates during MIS-13 inferred from correlating China loess and Antarctica ice records. *Clim Past*, 5(1), pp.21-31.

Hellstrom, J., 2006. U–Th dating of speleothems with high initial  $^{230}\text{Th}$  using stratigraphical constraint. *Quaternary Geochronology*, 1(4), pp.289-295.

International Hydropower Association, 2020. *2020 Hydropower Status Report*. [online] Available at: <<https://www.hydropower.org/country-profiles/region-east-asia-and-pacific>> [Accessed 18 August 2020].

Jaqueto, P., Trindade, R.I., Hartmann, G.A., Novello, V.F., Cruz, F.W., Karmann, I., Strauss, B.E. and Feinberg, J.M., 2016. Linking speleothem and soil magnetism in the Pau d'Alho cave (central South America). *Journal of Geophysical Research: Solid Earth*, 121(10), pp.7024-7039.

Kanner, L.C., Burns, S.J., Cheng, H., Edwards, R.L. and Vuille, M., 2013. High-resolution variability of the South American summer monsoon over the last seven millennia: insights from a speleothem record from the central Peruvian Andes. *Quaternary Science Reviews*, 75, pp.1-10.

Kaufmann, G., 2003. Stalagmite growth and palaeo-climate: the numerical perspective. *Earth and Planetary Science Letters*, 214(1-2), pp.251-266.

Kuo, T.S., Liu, Z.Q., Li, H.C., Wan, N.J., Shen, C.C. and Ku, T.L., 2011. Climate and environmental changes during the past millennium in central western Guizhou, China as recorded by Stalagmite ZJD-21. *Journal of Asian Earth Sciences*, 40(6), pp.1111-1120.

Liang, F., Brook, G.A., Kotlia, B.S., Railsback, L.B., Hardt, B., Cheng, H., Edwards, R.L. and Kandasamy, S., 2015. Panigarh cave stalagmite evidence of climate change in the Indian Central Himalaya since AD 1256: Monsoon breaks and winter southern jet depressions. *Quaternary Science Reviews*, 124, pp.145-161.

Li, H.C., Lee, Z.H., Wan, N.J., Shen, C.C., Li, T.Y., Yuan, D.X. and Chen, Y.H., 2011. The  $\delta^{18}\text{O}$  and  $\delta^{13}\text{C}$  records in an aragonite stalagmite from Furong Cave, Chongqing, China: A 2000-year record of monsoonal climate. *Journal of Asian Earth Sciences*, 40(6), pp.1121-1130.

Lisiecki, L.E. and Raymo, M.E., 2005. A Pliocene-Pleistocene stack of 57 globally distributed benthic  $\delta^{18}\text{O}$  records. *Paleoceanography*, 20(1).

Liu, L., Eronen, J.T. and Fortelius, M., 2009. Significant mid-latitude aridity in the middle Miocene of East Asia. *Palaeogeography, Palaeoclimatology, Palaeoecology*, 279(3-4), pp.201-206.

Magiera, M., Lechleitner, F.A., Erhardt, A.M., Hartland, A., Kwiecien, O., Cheng, H., Bradbury, H.J., Turchyn, A.V., Riechelmann, S., Edwards, L. and Breitenbach, S.F., 2019. Local and regional Indian Summer Monsoon precipitation dynamics during Termination II and the Last Interglacial. *Geophysical Research Letters*, 46(21), pp.12454-12463.

Mariethoz G, Kelly BF, Baker A. Quantifying the value of laminated stalagmites for paleoclimate reconstructions. *Geophysical research letters*. 2012 Mar;39(5).

Martín-Chivelet, J., Muñoz-García, M.B., Edwards, R.L., Turrero, M.J. and Ortega, A.I., 2011. Land surface temperature changes in Northern Iberia since 4000 yr BP, based on  $\delta^{13}C$  of speleothems. *Global and Planetary Change*, 77(1-2), pp.1-12.

Mikami, M., Shi, G.Y., Uno, I., Yabuki, S., Iwasaka, Y., Yasui, M., Aoki, T., Tanaka, T.Y., Kurosaki, Y., Masuda, K. and Uchiyama, A., 2006. Aeolian dust experiment on climate impact: An overview of Japan–China joint project ADEC. *Global and Planetary Change*, 52(1-4), pp.142-172.

Miller R.L., Knippertz P., Pérez García-Pando C., Perlwitz J.P., Tegen I. (2014) Impact of Dust Radiative Forcing upon Climate. In: Knippertz P., Stuut JB. (eds) *Mineral Dust*. Springer, Dordrecht

Robock, A., Mu, M., Vinnikov, K. and Robinson, D., 2003. Land surface conditions over Eurasia and Indian summer monsoon rainfall. *Journal of Geophysical Research: Atmospheres*, 108(D4).

Oxford University Press (2020 stalagmite. In: Lexico.com, Available at: <https://www.lexico.com/definition/stalagmite> [Accessed 14/06/2020].

Pausata, F.S., Battisti, D.S., Nisancioglu, K.H. and Bitz, C.M., 2011. Chinese stalagmite  $\delta^{18}O$  controlled by changes in the Indian monsoon during a simulated Heinrich event. *Nature Geoscience*, 4(7), pp.474-480.

Rohling, E.J., Liu, Q.S., Roberts, A.P., Stanford, J.D., Rasmussen, S.O., Langen, P.L. and Siddall, M., 2009. Controls on the East Asian monsoon during the last glacial cycle, based on comparison between Hulu Cave and polar ice-core records. *Quaternary Science Reviews*, 28(27-28), pp.3291-3302.

Siddall, M., Rohling, E.J., Almogi-Labin, A., Hemleben, C., Meischner, D., Schmelzer, I. and Smeed, D.A., 2003. Sea-level fluctuations during the last glacial cycle. *Nature*, 423(6942), pp.853-858.

Sletten, H.R., Railsback, L.B., Liang, F., Brook, G.A., Marais, E., Hardt, B.F., Cheng, H. and Edwards, R.L., 2013. A petrographic and geochemical record of climate change over the last 4600 years from a northern Namibia stalagmite, with evidence of abruptly wetter climate at the beginning of southern Africa's Iron Age. *Palaeogeography, Palaeoclimatology, Palaeoecology*, 376, pp.149-162.

Solace Global, 2018. *2018 South Asian Monsoon*. Travel Advisory - Environmental Risk. [online] Available at: <<https://www.solaceglobal.com/wp-content/uploads/2018/05/20180518-2018-South-Asia-Monsoon-Season-Travel-Advisory.pdf>> [Accessed 18 August 2020].

Statistics.laerd.com. n.d. *Spearman's Rank-Order Correlation - A Guide To When To Use It, What It Does And What The Assumptions Are.* [online] Available at: <<https://statistics.laerd.com/statistical-guides/spearmans-rank-order-correlation-statistical-guide.php>> [Accessed 15 August 2020].

Stoll, Heather. "30 years of the iron hypothesis of ice ages." (2020): 370-371.

Sun, H., Song, Y., Chen, X., Cheng, L. and Liu, H., 2020. Holocene dust deposition in the Ili Basin and its implications for climate variations in Westerlies-dominated Central Asia. *Palaeogeography, Palaeoclimatology, Palaeoecology*, 550, p.109731.

Sun, X. and Wang, P., 2005. How old is the Asian monsoon system?—Palaeobotanical records from China. *Palaeogeography, Palaeoclimatology, Palaeoecology*, 222(3-4), pp.181-222.

Toggweiler, J.R., 2009. Shifting westerlies. *Science*, 323(5920), pp.1434-1435.

Újvári, G., Kovács, J., Varga, G., Raucsik, B. and Marković, S.B., 2010. Dust flux estimates for the Last Glacial Period in East Central Europe based on terrestrial records of loess deposits: a review. *Quaternary Science Reviews*, 29(23-24), pp.3157-3166.

Waliser, D.E. and Gautier, C., 1993. A satellite-derived climatology of the ITCZ. *Journal of climate*, 6(11), pp.2162-2174.

Wang, P., Clemens, S., Beaufort, L., Braconnot, P., Ganssen, G., Jian, Z., Kershaw, P. and Sarnthein, M., 2005. Evolution and variability of the Asian monsoon system: state of the art and outstanding issues. *Quaternary Science Reviews*, 24(5-6), pp.595-629.

Wang, Y., Cheng, H., Edwards, R.L., Kong, X., Shao, X., Chen, S., Wu, J., Jiang, X., Wang, X. and An, Z., 2008. Millennial-and orbital-scale changes in the East Asian monsoon over the past 224,000 years. *Nature*, 451(7182), pp.1090-1093.

Wong, C.I. and Breecker, D.O., 2015. Advancements in the use of speleothems as climate archives. *Quaternary Science Reviews*, 127, pp.1-18.

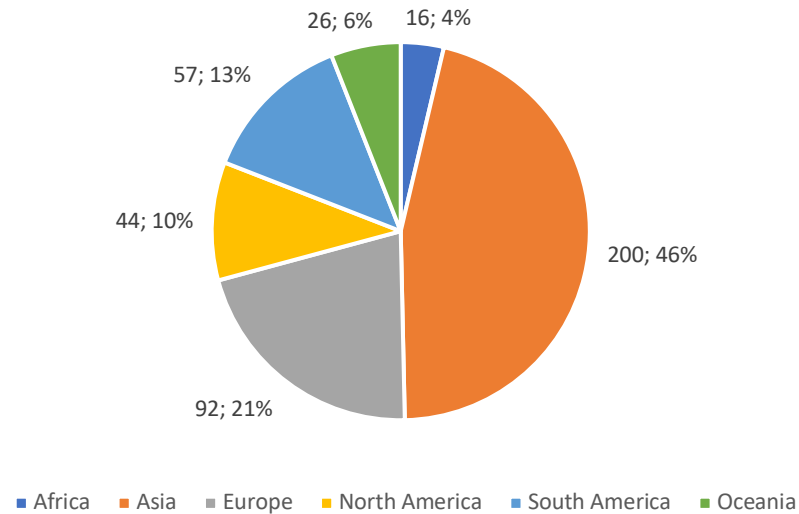
Yan, Y.Y., 2005. Intertropical convergence zone (ITCZ). *Encyclopedia of World Climatology*, pp.429-432.

Zhao, M., Li, H.C., Liu, Z.H., Mii, H.S., Sun, H.L., Shen, C.C. and Kang, S.C., 2015. Changes in climate and vegetation of central Guizhou in southwest China since the last glacial reflected by stalagmite records from Yelang Cave. *Journal of Asian Earth Sciences*, 114, pp.549-561.

## Appendix

### Appendix 1

Pie chart illustrating the distribution (absolute number; percentage) per continent (excluding Antarctica) of the 435 stalagmites collected for this study.



### Appendix 2

Table containing all 77 stalagmites that satisfied the two basic criteria. <sup>232</sup>Th concentrations highlighted in red were not used to calculate the mean value presented in the adjacent column as they were more than one standard deviation away from the mean. Stalagmites highlighted in blue were combined to calculate mean values for their respective caves.

Stalagmite Name	Location (Lat/Long)	Location (Cave)	Location (Country)	<sup>232</sup> Th (ppt)	Mean <sup>232</sup> Th (ppt) over 250 BP	Standard Deviation	Age (Yr)
10FC-02	-9.2919,159.5825	Forestry Cave	Solomon Islands	45	26	13	47
10FC-02	-9.2919,159.5825	Forestry Cave	Solomon Islands	47			57

10FC-02	-9.2919,159.5825	Forestry Cave	Solomon Islands	56			73
10FC-02	-9.2919,159.5825	Forestry Cave	Solomon Islands	19			80
10FC-02	-9.2919,159.5825	Forestry Cave	Solomon Islands	9			107
10FC-02	-9.2919,159.5825	Forestry Cave	Solomon Islands	36			108
10FC-02	-9.2919,159.5825	Forestry Cave	Solomon Islands	28			109
10FC-02	-9.2919,159.5825	Forestry Cave	Solomon Islands	15			123
10FC-02	-9.2919,159.5825	Forestry Cave	Solomon Islands	13			126
10FC-02	-9.2919,159.5825	Forestry Cave	Solomon Islands	38			147
10FC-02	-9.2919,159.5825	Forestry Cave	Solomon Islands	37			155
10FC-02	-9.2919,159.5825	Forestry Cave	Solomon Islands	50			157
10FC-02	-9.2919,159.5825	Forestry Cave	Solomon Islands	22			161
10FC-02	-9.2919,159.5825	Forestry Cave	Solomon Islands	11			161
10FC-02	-9.2919,159.5825	Forestry Cave	Solomon Islands	20			185
10FC-02	-9.2919,159.5825	Forestry Cave	Solomon Islands	29			187
10FC-02	-9.2919,159.5825	Forestry Cave	Solomon Islands	40			213
10FC-02	-9.2919,159.5825	Forestry Cave	Solomon Islands	10			233
10FC-02	-9.2919,159.5825	Forestry Cave	Solomon Islands	11			243
10FC-02	-9.2919,159.5825	Forestry Cave	Solomon Islands	35			255
10FC-02	-9.2919,159.5825	Forestry Cave	Solomon Islands	23			259
10FC-02	-9.2919,159.5825	Forestry Cave	Solomon Islands	13			263
10FC-02	-9.2919,159.5825	Forestry Cave	Solomon Islands	31			263
10FC-02	-9.2919,159.5825	Forestry Cave	Solomon Islands	23			270
10FC-02	-9.2919,159.5825	Forestry Cave	Solomon Islands	27			272
10FC-02	-9.2919,159.5825	Forestry Cave	Solomon Islands	26			272
10FC-02	-9.2919,159.5825	Forestry Cave	Solomon Islands	21			296
10FC-02	-9.2919,159.5825	Forestry Cave	Solomon Islands	8			302
10FC-02	-9.2919,159.5825	Forestry Cave	Solomon Islands	16			330

10FC-02	-9.2919,159.5825	Forestry Cave	Solomon Islands	22			348
10FC-02	-9.2919,159.5825	Forestry Cave	Solomon Islands	33			429
A1	29.29, 109.32	Lianhua Cave	China	732	754	1158	10
A1	29.29, 109.32	Lianhua Cave	China	2760			165
A1	29.29, 109.32	Lianhua Cave	China	776			307
AB-2	-15.54, 46.89	Anjohibe Cave	Madagascar	1204	922	1020	10
AB-2	-15.54, 46.89	Anjohibe Cave	Madagascar	496			157
AB-2	-15.54, 46.89	Anjohibe Cave	Madagascar	2867			420
AB-2	-15.54, 46.89	Anjohibe Cave	Madagascar	1067			455
ALH06	-15.1201,-56.4702	Pau d'Alho Cave	Brazil	10287	9835	3911	75
ALH06	-15.1201,-56.4702	Pau d'Alho Cave	Brazil	10317			158
ALH06	-15.1201,-56.4702	Pau d'Alho Cave	Brazil	8900			284
ALH06	-15.1201,-56.4702	Pau d'Alho Cave	Brazil	2125			368
BA03	4.03, 114.8	Bukit Assam cave	Malaysia	722	541	256	247
BA03	4.03, 114.8	Bukit Assam cave	Malaysia	360			263
C11	42.93,-4.35	Cueva del Cobre	Spain	16	19	14	77
C11	42.93,-4.35	Cueva del Cobre	Spain	42			303
C11	42.93,-4.35	Cueva del Cobre	Spain	21			472
C996-1	33.34,109.6	Jiuxian Cave	China	6505	3178	4311	160
C996-1	33.34,109.6	Jiuxian Cave	China	10278			190
C996-1	33.34,109.6	Jiuxian Cave	China	2340			290
C996-1	33.34,109.6	Jiuxian Cave	China	690			480
CAS-D	-6.053,-77.1330	Cascayunga Cave	Peru	1	5	23	112
CAS-D	-6.053,-77.1330	Cascayunga Cave	Peru	4			351
CAS-D	-6.053,-77.1330	Cascayunga Cave	Peru	50			421
CAS-D	-6.053,-77.1330	Cascayunga Cave	Peru	10			496
CNKS-3	42.52, 81.45	Kesang Cave	China	10281	4223	3502	130

CNKS-3	42.52, 81.45	Kesang Cave	China	4402			279
CNKS-3	42.52, 81.45	Kesang Cave	China	4043			424
CRC-3	36.59,-118.82	Crystal Cave	USA	933	1069	430	105
CRC-3	36.59,-118.82	Crystal Cave	USA	546			259
CRC-3	36.59,-118.82	Crystal Cave	USA	1563			265
CRC-3	36.59,-118.82	Crystal Cave	USA	1204			463
CRC-3	36.59,-118.82	Crystal Cave	USA	1204			463
CUR-4	-15.1220,-56.4841	Curupira Cave	Brazil	2591	1517	830	45
CUR-4	-15.1220,-56.4841	Curupira Cave	Brazil	1241			73
CUR-4	-15.1220,-56.4841	Curupira Cave	Brazil	638			120
CUR-4	-15.1220,-56.4841	Curupira Cave	Brazil	1792			185
D4	25.28,108.08	Dongge Cave	China	2	108	63	93
D4	25.28,108.08	Dongge Cave	China	94			183
D4	25.28,108.08	Dongge Cave	China	122			391
DX1	25.17, 108.05	Dongge Cave	China	144	194	90	13
DX1	25.17, 108.05	Dongge Cave	China	308			61
DX1	25.17, 108.05	Dongge Cave	China	204			162
DX1	25.17, 108.05	Dongge Cave	China	176			215
DX1	25.17, 108.05	Dongge Cave	China	57			234
DX1	25.17, 108.05	Dongge Cave	China	272			381
DAN-D	19, 82	Dandak cave	India	1313	1946	1505	447
DAN-D	19, 82	Dandak cave	India	860			455
DAN-D	19, 82	Dandak cave	India	3664			497
DV2	-12.22,-41.34	Diva de Maura Cave	Brazil	555	346	191	100
DV2	-12.22,-41.34	Diva de Maura Cave	Brazil	421			148
DV2	-12.22,-41.34	Diva de Maura Cave	Brazil	171			240

DV2	-12.22,-41.34	Diva de Maura Cave	Brazil	447			396
DV2	-12.22,-41.34	Diva de Maura Cave	Brazil	110			457
DY-1	33.08,106.18	Dayu Cave	China	400	495	219	114
DY-1	33.08,106.18	Dayu Cave	China	585			163
DY-1	33.08,106.18	Dayu Cave	China	612			290
DY-1	33.08,106.18	Dayu Cave	China	384			391
DY-1	33.08,106.18	Dayu Cave	China	927			438
ELC-A	-5.56,-77.18	El Condor Cave	Peru	1170			1040
ELC-A	-5.56,-77.18	El Condor Cave	Peru	910	393		
FN1	-5.36, -37.44	Furna Nova	Brazil	228	463	1986	323
FN1	-5.36, -37.44	Furna Nova	Brazil	698			328
FN1	-5.36, -37.44	Furna Nova	Brazil	3878			500
FR0510-1	29.13,107.54	Furong Cave	China	8356	11411	2082	322
FR0510-1	29.13,107.54	Furong Cave	China	9416			327
FR0510-1	29.13,107.54	Furong Cave	China	12537			351
FR0510-1	29.13,107.54	Furong Cave	China	12281			455
Gej-1	35.8044, 49.1645	Gejkar Cave	Iraq	684	635	69	125
Gej-1	35.8044, 49.1646	Gejkar Cave	Iraq	586			421
H12	23.05,57.21	Hoti Cave	Oman	6939	10488	5018	230
H12	23.05,57.21	Hoti Cave	Oman	14036			450
HY1	33.35,105.07	Huangye Cave	China	2534	3091	4245	4
HY1	33.35,105.07	Huangye Cave	China	2968			48
HY1	33.35,105.07	Huangye Cave	China	1961			78
HY1	33.35,105.07	Huangye Cave	China	826			134
HY1	33.35,105.07	Huangye Cave	China	3927			164
HY1	33.35,105.07	Huangye Cave	China	14142			451



HY1	33.35,105.07	Huangye Cave	China	6330			460
HY3	33.35,105.07	Huangye Cave	China	2656			434
JHU-1	18.52,81.52	Jhumar Cave	India	2030	2050	95	24
JHU-1	18.52,81.52	Jhumar Cave	India	1890			154
JHU-1	18.52,81.52	Jhumar Cave	India	2070			224
JX-1	17.4,-99.2	Juxtlahuaca Cave	Mexico	423	863	10422	102
JX-1	17.4,-99.2	Juxtlahuaca Cave	Mexico	21693			115
JX-1	17.4,-99.2	Juxtlahuaca Cave	Mexico	844			210
JX-1	17.4,-99.2	Juxtlahuaca Cave	Mexico	1321			335
KNI-51 G	-15.18,128.37	Cave KNI-51	Australia	1393	973	715	314
KNI-51 G	-15.18,128.37	Cave KNI-51	Australia	2248			338
KNI-51 G	-15.18,128.37	Cave KNI-51	Australia	604			378
KNI-51 G	-15.18,128.37	Cave KNI-51	Australia	921			435
LC-1	37.8,-115.6	Leviathan Cave	USA	696	640	79	317
LC-1	37.8,-115.6	Leviathan Cave	USA	584			491
LD12	-12.2,-41.36	Lapa Doce Cave	Brazil	249	232	136	13
LD12	-12.2,-41.36	Lapa Doce Cave	Brazil	350			16
LD12	-12.2,-41.36	Lapa Doce Cave	Brazil	188			28
LD12	-12.2,-41.36	Lapa Doce Cave	Brazil	523			29
LD12	-12.2,-41.36	Lapa Doce Cave	Brazil	210			53
LD12	-12.2,-41.36	Lapa Doce Cave	Brazil	162			90
LH2	29.29,109.32	Lianhua Cave	China	842	520	318	51
LH2	29.29,109.32	Lianhua Cave	China	610			144
LH2	29.29,109.32	Lianhua Cave	China	89			290
LH2	29.29,109.32	Lianhua Cave	China	429			479
LR06-B1	-8.32, 120.26	Liang Luar Cave	Indonesia	42	45	4	337
LR06-B1	-8.32, 120.26	Liang Luar Cave	Indonesia	50			-39

LR06-B1	-8.32, 120.26	Liang Luar Cave	Indonesia	42			337
LR06-B1	-8.32, 120.26	Liang Luar Cave	Indonesia	24			801
LR06-B3	-8.32, 120.26	Liang Luar Cave	Indonesia	47			53
LS-9602	39.47, 115.56	ShiHua Cave	China	125	149	34	63
LS-9602	39.47, 115.56	ShiHua Cave	China	173			294
TS-9701	39.47, 115.56	ShiHua Cave	China	603	760	223	52
TS-9701	39.47, 115.56	ShiHua Cave	China	918			454
MA2	-52.41,-73.23	Marcelo Arévalo Cave	Chile	1091	1750	6038	96
MA2	-52.41,-73.23	Marcelo Arévalo Cave	Chile	2409			411
MA2	-52.41,-73.23	Marcelo Arévalo Cave	Chile	12145			498
MC01	16.83,-89.1	Macal Chasm	Belize	2984	2321	938	253
MC01	16.83,-89.1	Macal Chasm	Belize	1658			443
N1	31.42, 110.16	Niu Cave	China	613	455	223	82
N1	31.42, 110.16	Niu Cave	China	297			265
P00-H1	-11.27,-75.79	Huagapo Cave	Peru	131	387	361	132
P00-H1	-11.27,-75.79	Huagapo Cave	Peru	642			423
PAL3	-5.92, -77.35	Palestina Cave	Peru	499	153	175	134
PAL3	-5.92, -77.35	Palestina Cave	Peru	185			226
PAL3	-5.92, -77.35	Palestina Cave	Peru	149			339
PAL3	-5.92, -77.35	Palestina Cave	Peru	126			488
PAL4	-5.92, -77.35	Palestina Cave	Peru	1575	262	592	224
PAL4	-5.92, -77.35	Palestina Cave	Peru	131			239
PAL4	-5.92, -77.35	Palestina Cave	Peru	293			300
PAL4	-5.92, -77.35	Palestina Cave	Peru	307			412
PAL4	-5.92, -77.35	Palestina Cave	Peru	316			499

PGH-1	29.33,80.07	Panigarh Cave	India	4027	3460	802	31
PGH-1	29.33,80.07	Panigarh Cave	India	2893			291
PP1	32.05,-105.1	Pink Panther Cave	USA	2380	1539	501	300
PP1	32.05,-105.1	Pink Panther Cave	USA	1662			337
PP1	32.05,-105.1	Pink Panther Cave	USA	1416			346
S3	17.07, 54.05	Kahf Defore	Oman	206	310	147	210
S3	17.07, 54.05	Kahf Defore	Oman	414			460
SAH-A	30.6, 77.8667	Sahiya cave	India	127	545	1115	30
SAH-A	30.6, 77.8667	Sahiya cave	India	2974			77
SAH-A	30.6, 77.8667	Sahiya cave	India	1055			176
SAH-A	30.6, 77.8667	Sahiya cave	India	185			245
SAH-A	30.6, 77.8667	Sahiya cave	India	1273			309
SAH-A	30.6, 77.8667	Sahiya cave	India	86			367
SLX1	42.3,-3.53	Cueva Mayor	Spain	125	130	390	81
SLX1	42.3,-3.53	Cueva Mayor	Spain	13			115
SLX1	42.3,-3.53	Cueva Mayor	Spain	243			206
SLX1	42.3,-3.53	Cueva Mayor	Spain	138			226
SLX1	42.3,-3.53	Cueva Mayor	Spain	982			328
SN20	28.42, 117.15	Shennong Cave	China	622	709	323	102
SN20	28.42, 117.15	Shennong Cave	China	570			226
SN20	28.42, 117.15	Shennong Cave	China	936			491
SN20	28.42, 117.15	Shennong Cave	China	1268			25
SN4	28.42, 117.15	Shennong Cave	China	1325	803	738	248
SN4	28.42, 117.15	Shennong Cave	China	281			437
So-1	41.25,31.56	Sofular Cave	Turkey	152	216	38	248
So-1	41.25,31.56	Sofular Cave	Turkey	211			494
So-10	41.25,31.56	Sofular Cave	Turkey	221			283

SPA12	47.11,11.56	Spannagel Cave	Austria	2364	857	914	64		
SPA12	47.11,11.56	Spannagel Cave	Austria	576			230		
SPA12	47.11,11.56	Spannagel Cave	Austria	1138			382		
SVC982	43.44,-92.24	Spring Valley Caverns	USA	3306	97	1853	60		
SVC982	43.44,-92.24	Spring Valley Caverns	USA	86			225		
SVC982	43.44,-92.24	Spring Valley Caverns	USA	108			310		
TR5	-12.2,-41.36	Torrinha Cave	Brazil	128	163	357	12		
TR5	-12.2,-41.36	Torrinha Cave	Brazil	107			20		
TR5	-12.2,-41.36	Torrinha Cave	Brazil	174			23		
TR5	-12.2,-41.36	Torrinha Cave	Brazil	138			27		
TR5	-12.2,-41.36	Torrinha Cave	Brazil	115			31		
TR5	-12.2,-41.36	Torrinha Cave	Brazil	79			37		
TR5	-12.2,-41.36	Torrinha Cave	Brazil	167			46		
TR5	-12.2,-41.36	Torrinha Cave	Brazil	279			97		
TR5	-12.2,-41.36	Torrinha Cave	Brazil	341			131		
TR5	-12.2,-41.36	Torrinha Cave	Brazil	102			137		
TR5	-12.2,-41.36	Torrinha Cave	Brazil	1316			164		
TUL	29.53,79.21	Chulerasim Cave	India	9308			7363	4525	43
TUL	29.53,79.21	Chulerasim Cave	India	286					182
TUL	29.53,79.21	Chulerasim Cave	India	5417	307				
vil-stm1	45.26,0.47	Villars Cave	France	202	119	117	117		
vil-stm1	45.26,0.47	Villars Cave	France	36			385		
WH9801	32.11,-104.59	Carlsbad Cavern	USA	564	727	230	471		
WH9801	32.11,-104.59	Carlsbad Cavern	USA	889			474		
WS-B	25.15,91.52	Wah Shikar Cave	Bangladesh	284	1313	4509	144		

WS-B	25.15,91.52	Wah Shikar Cave	Bangladesh	2440			200
WS-B	25.15,91.52	Wah Shikar Cave	Bangladesh	870			224
WS-B	25.15,91.52	Wah Shikar Cave	Bangladesh	1130			255
WS-B	25.15,91.52	Wah Shikar Cave	Bangladesh	1750			385
WS-B	25.15,91.52	Wah Shikar Cave	Bangladesh	8400			440
WS-B	25.15,91.52	Wah Shikar Cave	Bangladesh	2360			460
WS-B	25.15,91.52	Wah Shikar Cave	Bangladesh	670			467
WS-B	25.15,91.52	Wah Shikar Cave	Bangladesh	14300			470
WS-B	25.15,91.52	Wah Shikar Cave	Bangladesh	1000			473
WX42B	33.19,105	Wanxiang Cave	China	2240			525
WX42B	33.19,105	Wanxiang Cave	China	350	53		
WX42B	33.19,105	Wanxiang Cave	China	260	82		
WX42B	33.19,105	Wanxiang Cave	China	240	241		
WX42B	33.19,105	Wanxiang Cave	China	1250	348		
YOK-G	16.30, -89.4	Yok Balum	Belize	58	29	37	28
YOK-G	16.30, -89.4	Yok Balum	Belize	27			50
YOK-G	16.30, -89.4	Yok Balum	Belize	7			72
YOK-G	16.30, -89.4	Yok Balum	Belize	31			119
YOK-G	16.30, -89.4	Yok Balum	Belize	117			137
YOK-G	16.30, -89.4	Yok Balum	Belize	4			166
YOK-G	16.30, -89.4	Yok Balum	Belize	35			189
YOK-G	16.30, -89.4	Yok Balum	Belize	17			208
YOK-G	16.30, -89.4	Yok Balum	Belize	5			228
YOK-G	16.30, -89.4	Yok Balum	Belize	8			248
YOK-G	16.30, -89.4	Yok Balum	Belize	49			278
YOK-G	16.30, -89.4	Yok Balum	Belize	64			296
YOK-G	16.30, -89.4	Yok Balum	Belize	80			330

YOK-G	16.30, -89.4	Yok Balum	Belize	14			348
YOK-G	16.30, -89.4	Yok Balum	Belize	106			372
ZJD-21	26.4, 105.46	Zhijin Cave	China	163			88
ZJD-21	26.4, 105.46	Zhijin Cave	China	375	269	427	163
ZJD-21	26.4, 105.46	Zhijin Cave	China	986			331
Y04-CH	20.73, -89.72	Tzabnah Cave	Mexico	491			5.6
Y04-CH	20.73, -89.72	Tzabnah Cave	Mexico	753			109.6
Y04-CH	20.73, -89.72	Tzabnah Cave	Mexico	337	379	251	284.2
Y04-CH	20.73, -89.72	Tzabnah Cave	Mexico	310			466.3
Y04-CH	20.73, -89.72	Tzabnah Cave	Mexico	72			491.3
PDR-1	18, -67	Perdida Cave	Puerto Rico	150			-55
PDR-1	18, -67	Perdida Cave	Puerto Rico	4			61
PDR-1	18, -67	Perdida Cave	Puerto Rico	2			177
PDR-1	18, -67	Perdida Cave	Puerto Rico	1640	222	658	345
PDR-1	18, -67	Perdida Cave	Puerto Rico	837			383
PDR-1	18, -67	Perdida Cave	Puerto Rico	117			418
GU-Xi-1	16.5, -89.0	Xibalba Cave	Belize	105			-17.2
GU-Xi-1	16.5, -89.0	Xibalba Cave	Belize	819			43.5
GU-Xi-1	16.5, -89.0	Xibalba Cave	Belize	225			88
GU-Xi-1	16.5, -89.0	Xibalba Cave	Belize	209			118.5
GU-Xi-1	16.5, -89.0	Xibalba Cave	Belize	216	186	260	154
GU-Xi-1	16.5, -89.0	Xibalba Cave	Belize	334			185.9
GU-Xi-1	16.5, -89.0	Xibalba Cave	Belize	11			209.7
GU-Xi-1	16.5, -89.0	Xibalba Cave	Belize	545			236
GU-Xi-1	16.5, -89.0	Xibalba Cave	Belize	28			272.7
MAJ-5	-15.58, 46.73	Anjokipoty Cave	Madagascar	3044			150
MAJ-5	-15.58, 46.73	Anjokipoty Cave	Madagascar	22757	12901	13939	446

Taurus	-15.53, 167.02	Taurus Cave	Vanuatu	79	39	16	38
Taurus	-15.53, 167.02	Taurus Cave	Vanuatu	74			19
Taurus	-15.53, 167.02	Taurus Cave	Vanuatu	40			117
Taurus	-15.53, 167.02	Taurus Cave	Vanuatu	33			62
Taurus	-15.53, 167.02	Taurus Cave	Vanuatu	34			73
Taurus	-15.53, 167.02	Taurus Cave	Vanuatu	33			44
Taurus	-15.53, 167.02	Taurus Cave	Vanuatu	44			77
Taurus	-15.53, 167.02	Taurus Cave	Vanuatu	29			73
Taurus	-15.53, 167.02	Taurus Cave	Vanuatu	76			129
Taurus	-15.53, 167.02	Taurus Cave	Vanuatu	39			36
Taurus	-15.53, 167.02	Taurus Cave	Vanuatu	42			86
Taurus	-15.53, 167.02	Taurus Cave	Vanuatu	25			106
Taurus	-15.53, 167.02	Taurus Cave	Vanuatu	34			109
Taurus	-15.53, 167.02	Taurus Cave	Vanuatu	41			128
Taurus	-15.53, 167.02	Taurus Cave	Vanuatu	71			141
Taurus	-15.53, 167.02	Taurus Cave	Vanuatu	25			160
Taurus	-15.53, 167.02	Taurus Cave	Vanuatu	44			174
Taurus	-15.53, 167.02	Taurus Cave	Vanuatu	46			195
Taurus	-15.53, 167.02	Taurus Cave	Vanuatu	39			203
Taurus	-15.53, 167.02	Taurus Cave	Vanuatu	41			217
Taurus	-15.53, 167.02	Taurus Cave	Vanuatu	61			220
Taurus	-15.53, 167.02	Taurus Cave	Vanuatu	34			230
Taurus	-15.53, 167.02	Taurus Cave	Vanuatu	20			246
Taurus	-15.53, 167.02	Taurus Cave	Vanuatu	50			270
Taurus	-15.53, 167.02	Taurus Cave	Vanuatu	39			266
Taurus	-15.53, 167.02	Taurus Cave	Vanuatu	51			287
Taurus	-15.53, 167.02	Taurus Cave	Vanuatu	28			330

Taurius	-15.53, 167.02	Taurius Cave	Vanuatu	22			338
Taurius	-15.53, 167.02	Taurius Cave	Vanuatu	26			359
Taurius	-15.53, 167.02	Taurius Cave	Vanuatu	33			381
IFK1	30.71, -9.33	Ifoulki Cave	Morocco	315			25
IFK1	30.71, -9.33	Ifoulki Cave	Morocco	61			53
IFK1	30.71, -9.33	Ifoulki Cave	Morocco	105			69
IFK1	30.71, -9.33	Ifoulki Cave	Morocco	80			134
IFK1	30.71, -9.33	Ifoulki Cave	Morocco	273			159
IFK1	30.71, -9.33	Ifoulki Cave	Morocco	564	188	166	282
IFK1	30.71, -9.33	Ifoulki Cave	Morocco	183			368
IFK1	30.71, -9.33	Ifoulki Cave	Morocco	170			417
IFK1	30.71, -9.33	Ifoulki Cave	Morocco	464			446
IFK1	30.71, -9.33	Ifoulki Cave	Morocco	189			493
PAR03	-4.07, -55.45	Paraiso Cave	Brazil	91			4
PAR03	-4.07, -55.45	Paraiso Cave	Brazil	34	69	189	55
PAR03	-4.07, -55.45	Paraiso Cave	Brazil	81			202
PAR03	-4.07, -55.45	Paraiso Cave	Brazil	443			403
TM0	-16, -47	Tamboril Cave	Brazil	112			95
TM0	-16, -47	Tamboril Cave	Brazil	745			134
TM0	-16, -47	Tamboril Cave	Brazil	25	130	293	142
TM0	-16, -47	Tamboril Cave	Brazil	84			329
TM0	-16, -47	Tamboril Cave	Brazil	297			416
TM2	-16, -47	Tamboril Cave	Brazil	762			248
TM2	-16, -47	Tamboril Cave	Brazil	414	588	246	492
SBE3	-13.81, -46.35	Sao Bernardo Cave	Brazil	21914			74
SBE3	-13.81, -46.35	Sao Bernardo Cave	Brazil	165	182	9720	131
SBE3	-13.81, -46.35	Sao Bernardo Cave	Brazil	135			246



SBE3	-13.81, -46.35	Sao Bernardo Cave	Brazil	356			303
SBE3	-13.81, -46.35	Sao Bernardo Cave	Brazil	71			467
Sha-2	-5.7, -77.9	Shatuca Cave	Peru	186	154	46	263
Sha-2	-5.7, -77.9	Shatuca Cave	Peru	121			399
MC08-01	56.58, -119.65	Minnetonka Cave	Canada	499	112	201	26
MC08-01	56.58, -119.65	Minnetonka Cave	Canada	185			107
MC08-01	56.58, -119.65	Minnetonka Cave	Canada	91			292
MC08-01	56.58, -119.65	Minnetonka Cave	Canada	60			420
Uluu2	40.40, 72.35	Uluu-Too Cave	Kyrgystan	286	374	287	70
Uluu2	40.40, 72.35	Uluu-Too Cave	Kyrgystan	461			158
Uluu2	40.40, 72.35	Uluu-Too Cave	Kyrgystan	847			178
Mun-stm2	15.15, 77.92	Munagamana Cave	India	2496	568	703	427
Mun-stm2	15.15, 77.92	Munagamana Cave	India	527			293
Mun-stm2	15.15, 77.92	Munagamana Cave	India	112			282
Mun-stm2	15.15, 77.92	Munagamana Cave	India	573			275
Mun-stm2	15.15, 77.92	Munagamana Cave	India	324			172
Mun-stm2	15.15, 77.92	Munagamana Cave	India	1095			135
Mun-stm2	15.15, 77.92	Munagamana Cave	India	786			101
Mun-stm2	15.15, 77.92	Munagamana Cave	India	719			64
Mun-stm2	15.15, 77.92	Munagamana Cave	India	407			1
Mun-stm1	15.15, 77.92	Munagamana Cave	India	837			879
Mun-stm1	15.15, 77.92	Munagamana Cave	India	2106	537		
Mun-stm1	15.15, 77.92	Munagamana Cave	India	694	405		
Mun-stm1	15.15, 77.92	Munagamana Cave	India	367	311		
Mun-stm1	15.15, 77.92	Munagamana Cave	India	1190	240		
Mun-stm1	15.15, 77.92	Munagamana Cave	India	1109	305		
Mun-stm1	15.15, 77.92	Munagamana Cave	India	5632	166		

Mun-stm1	15.15, 77.92	Munagamana Cave	India	232			68
Mun-stm1	15.15, 77.92	Munagamana Cave	India	498			41
C09-2	45.1, 22.8	Closani Cave	Romania	27			117
C09-2	45.1, 22.8	Closani Cave	Romania	19	28	5	352
C09-2	45.1, 22.8	Closani Cave	Romania	29			476
DP1	-19.24,17.53	Dante Cave	Namibia	209			14
DP1	-19.24,17.53	Dante Cave	Namibia	37	36	100	143
DP1	-19.24,17.53	Dante Cave	Namibia	34			382
20120824-13	26.228,105.441	Yelang Cave	China	130			393
20120824-13	26.228,105.441	Yelang Cave	China	22	76	525	218689
20120824-13	26.228,105.441	Yelang Cave	China	981			-111
WIN2	30.77, -9.49	Wintimdouine Cave	Morocco	695			27
WIN2	30.77, -9.49	Wintimdouine Cave	Morocco	1359	2304	1671	45
WIN2	30.77, -9.49	Wintimdouine Cave	Morocco	2237			106
WIN2	30.77, -9.49	Wintimdouine Cave	Morocco	5288			157
WIN2	30.77, -9.49	Wintimdouine Cave	Morocco	3637			359
WIN2	30.77, -9.49	Wintimdouine Cave	Morocco	1984			416
WIN3	30.77, -9.49	Wintimdouine Cave	Morocco	2022	2304 1863	1671 873	203
WIN3	30.77, -9.49	Wintimdouine Cave	Morocco	3349			381
WIN3	30.77, -9.49	Wintimdouine Cave	Morocco	1704			487

### Appendix 3

This table highlights the 4 compiled cave data sets (due to overlapping DCMD data source areas) and the stalagmites and caves that contributed. Different colors denote different compiled data sets. <sup>232</sup>Th concentrations highlighted in red were not used to calculate mean values.

Stalagmite Name	Location (Lat/Long)	Cave	Country	<sup>232</sup> Th (ppt)	Mean <sup>232</sup> Th (ppt)	Median <sup>232</sup> Th (ppt)	Standard Deviation	Age(Yr)			
ELC-A	-5.56,-77.18	El Condor Cave	Peru	1170	355	185	448	373			
ELC-A	-5.56,-77.18	El Condor Cave	Peru	910				393			
Sha-2	-5.7, -77.9	Shatuca Cave	Peru	186				263			
Sha-2	-5.7, -77.9	Shatuca Cave	Peru	121				399			
PAL4	-5.92, -77.35	Palestina Cave	Peru	1575				224			
PAL4	-5.92, -77.35	Palestina Cave	Peru	131				239			
PAL4	-5.92, -77.35	Palestina Cave	Peru	293				300			
PAL4	-5.92, -77.35	Palestina Cave	Peru	307				412			
PAL4	-5.92, -77.35	Palestina Cave	Peru	316				499			
PAL3	-5.92, -77.35	Palestina Cave	Peru	499				134			
PAL3	-5.92, -77.35	Palestina Cave	Peru	185				226			
PAL3	-5.92, -77.35	Palestina Cave	Peru	149				339			
PAL3	-5.92, -77.35	Palestina Cave	Peru	126				488			
CAS-D	-6.05,-77.13	Cascayunga Cave	Peru	1				112			
CAS-D	-6.05,-77.13	Cascayunga Cave	Peru	4				351			
CAS-D	-6.05,-77.13	Cascayunga Cave	Peru	50				421			
CAS-D	-6.05,-77.13	Cascayunga Cave	Peru	10				496			
GU-Xi-1	16.5, -89.0	Xibalba Cave	Belize	105				67	54	195	-17.2
GU-Xi-1	16.5, -89.0	Xibalba Cave	Belize	819							43.5
GU-Xi-1	16.5, -89.0	Xibalba Cave	Belize	225							88
GU-Xi-1	16.5, -89.0	Xibalba Cave	Belize	209	118.5						
GU-Xi-1	16.5, -89.0	Xibalba Cave	Belize	216	154						

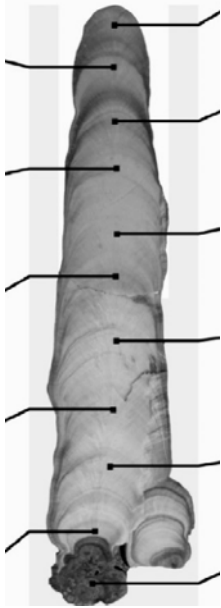
GU-Xi-1	16.5, -89.0	Xibalba Cave	Belize	334				185.9
GU-Xi-1	16.5, -89.0	Xibalba Cave	Belize	11				209.7
GU-Xi-1	16.5, -89.0	Xibalba Cave	Belize	545				236
GU-Xi-1	16.5, -89.0	Xibalba Cave	Belize	28				272.7
YOK-G	16.30, -89.4	Yok Balum	Belize	58				28
YOK-G	16.30, -89.4	Yok Balum	Belize	27				50
YOK-G	16.30, -89.4	Yok Balum	Belize	7				72
YOK-G	16.30, -89.4	Yok Balum	Belize	31				119
YOK-G	16.30, -89.4	Yok Balum	Belize	117				137
YOK-G	16.30, -89.4	Yok Balum	Belize	4				166
YOK-G	16.30, -89.4	Yok Balum	Belize	35				189
YOK-G	16.30, -89.4	Yok Balum	Belize	17				208
YOK-G	16.30, -89.4	Yok Balum	Belize	5				228
YOK-G	16.30, -89.4	Yok Balum	Belize	8				248
YOK-G	16.30, -89.4	Yok Balum	Belize	49				278
YOK-G	16.30, -89.4	Yok Balum	Belize	64				296
YOK-G	16.30, -89.4	Yok Balum	Belize	80				330
YOK-G	16.30, -89.4	Yok Balum	Belize	14				348
YOK-G	16.30, -89.4	Yok Balum	Belize	106				372
LD12	-12.2,-41.36	Lapa Doce Cave	Brazil	249				239
LD12	-12.2,-41.36	Lapa Doce Cave	Brazil	350	16			
LD12	-12.2,-41.36	Lapa Doce Cave	Brazil	188	28			
LD12	-12.2,-41.36	Lapa Doce Cave	Brazil	523	29			
LD12	-12.2,-41.36	Lapa Doce Cave	Brazil	210	53			
LD12	-12.2,-41.36	Lapa Doce Cave	Brazil	162	90			
DV2	-12.22,-41.34	Diva de Maura Cave	Brazil	555	100			

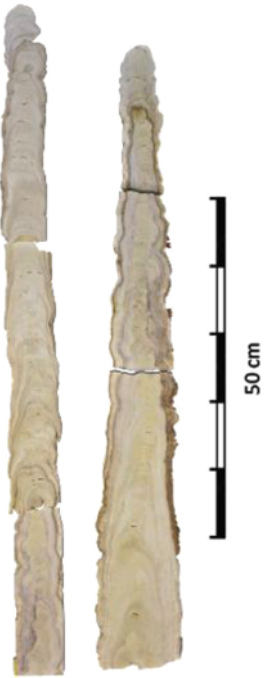
DV2	-12.22,-41.34	Diva de Maura Cave	Brazil	421				148
DV2	-12.22,-41.34	Diva de Maura Cave	Brazil	171				240
DV2	-12.22,-41.34	Diva de Maura Cave	Brazil	447				396
DV2	-12.22,-41.34	Diva de Maura Cave	Brazil	110				457
TR5	-12.2,-41.36	Torrinha Cave	Brazil	128				12
TR5	-12.2,-41.36	Torrinha Cave	Brazil	107				20
TR5	-12.2,-41.36	Torrinha Cave	Brazil	174				23
TR5	-12.2,-41.36	Torrinha Cave	Brazil	138				27
TR5	-12.2,-41.36	Torrinha Cave	Brazil	115				31
TR5	-12.2,-41.36	Torrinha Cave	Brazil	79				37
TR5	-12.2,-41.36	Torrinha Cave	Brazil	167				46
TR5	-12.2,-41.36	Torrinha Cave	Brazil	279				97
TR5	-12.2,-41.36	Torrinha Cave	Brazil	341				131
TR5	-12.2,-41.36	Torrinha Cave	Brazil	102				137
TR5	-12.2,-41.36	Torrinha Cave	Brazil	1316				164
HY1	33.35,105.07	Huangye Cave	China	2534	2081	2101	3906	4
HY1	33.35,105.07	Huangye Cave	China	2968				48
HY1	33.35,105.07	Huangye Cave	China	1961				78
HY1	33.35,105.07	Huangye Cave	China	826				134
HY1	33.35,105.07	Huangye Cave	China	3927				164
HY1	33.35,105.07	Huangye Cave	China	14142				451
HY1	33.35,105.07	Huangye Cave	China	6330				460
WX42B	33.19,105	Wanxiang Cave	China	2240				7
WX42B	33.19,105	Wanxiang Cave	China	350				53
WX42B	33.19,105	Wanxiang Cave	China	260				82

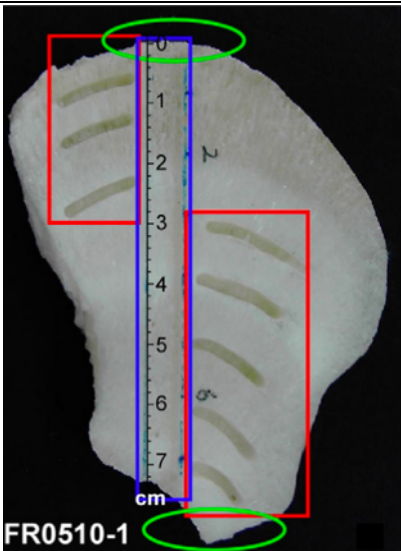
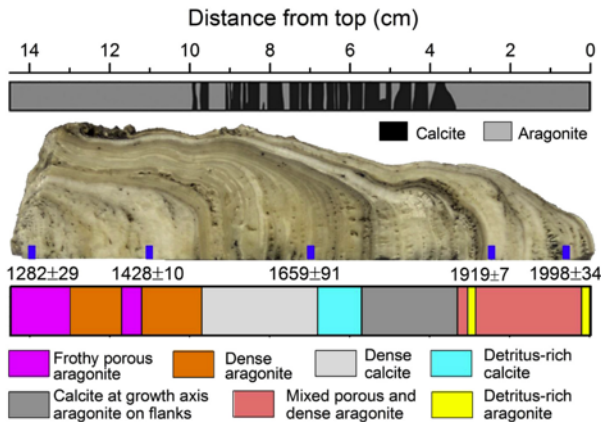
WX42B	33.19,105	Wanxiang Cave	China	240				241
WX42B	33.19,105	Wanxiang Cave	China	1250				348

#### Appendix 4

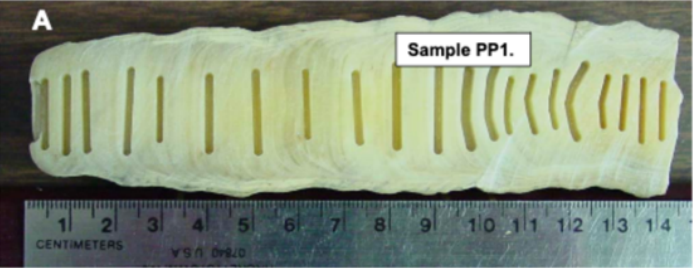
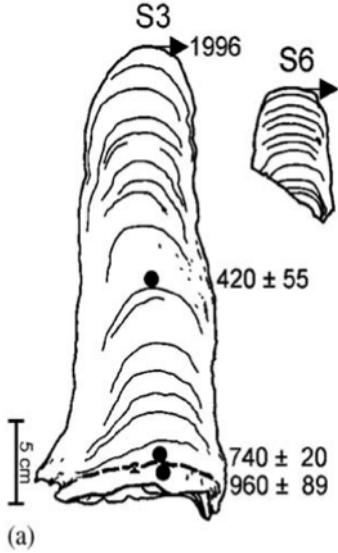
Table containing details on disregarded stalagmites.


Stalagmite	Cave, Country	Lat/Longitude	Reason Stalagmite was disregarded	Picture of Stalagmite
LH2	Lianhua, China	109°32 E, 29°29 N	Lianhua cave was discovered during roadworks in 2006 and was previously completely sealed off, disabling any interaction with the outside atmosphere. For this reason, $^{232}\text{Th}$ concentrations measured in LH2 alliquots could not be representative of DCMD measurements.	

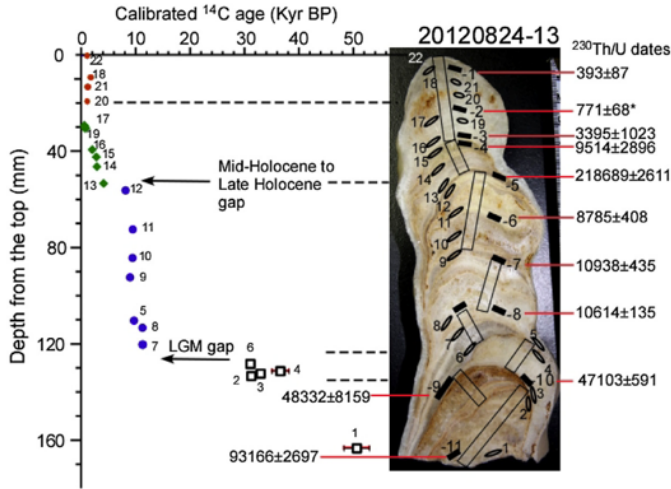
AB-2	Anjohibe, Madagascar	46°89 E, 15°54 S	Burns et al. (2016) used Osmond Type II constructed isochrons to determine an initial $^{230}\text{Th}/^{232}\text{Th}$ ratio. The use of isochrons is indicative of unreliable or tricky stalagmites and all stalagmites that have required the drilling of isochrons were removed from the correlation curve.	 <p data-bbox="1563 890 1702 912">Ab-2 Ab-3</p> <p data-bbox="1653 976 1702 1008">NA</p>
BA03	Bukit Assam, Malaysian Borneo	114° E, 4° N	Stalagmite BA03 was removed due to the use of isochrons in Chen et al.'s 2016 study.	

FR0510-1	Furong, China	107°54 E, 29°13 N	Li et al. (2011) state that isochron dating techniques were used on two layers, at depths of 4mm and 20mm. For this reason, the FR0510-1 stalagmite was disqualified from the correlation curve.	
PGH-1	Panigarh, India	80°07'03 E, 29°33'10 N	Column 5 shows a figure taken from Liang et al's (2015) paper published in Quaternary Science Reviews. This figure illustrates very detritus rich calcite and aragonite composition up to a depth of approximately 3 centimeters. This detrital contamination renders the <sup>232</sup> Th values from this stalagmite unreliable as a representation of suspended aerosols blown into the cave's atmosphere.	 <p>Distance from top (cm)</p> <p>14 12 10 8 6 4 2 0</p> <p>■ Calcite ■ Aragonite</p> <p>1282±29 1428±10 1659±91 1919±7 1998±34</p> <p>     ■ Frothy porous aragonite   ■ Dense aragonite   ■ Dense calcite   ■ Detritus-rich calcite      ■ Calcite at growth axis aragonite on flanks   ■ Mixed porous and dense aragonite   ■ Detritus-rich aragonite   </p>

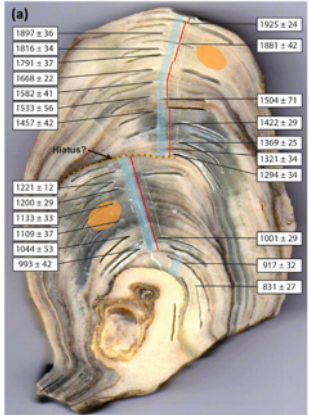
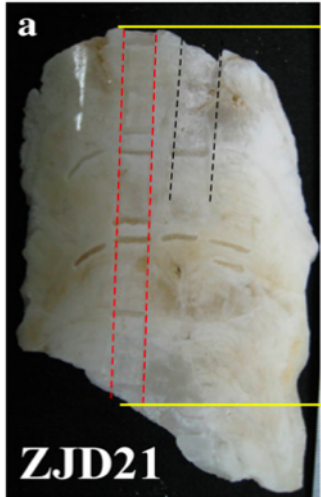


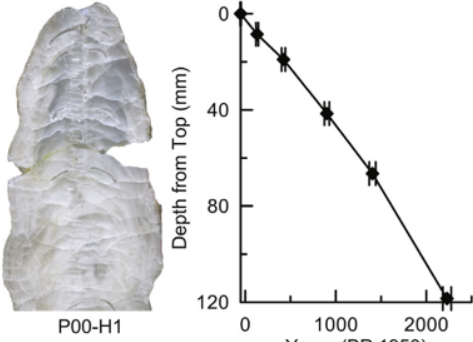

PP1	Pink Panther, USA	NA	Very large dating errors make it impossible to guarantee that $^{232}\text{Th}$ concentrations are from the last 500 years. Without the ability to guarantee multiple data points within this time period PP1 cannot be included in the correlation plot.	
S3	Kahf Defore, Oman	54°05 E, 17°07 N,	Two large age reversals in samples taken from the top of the stalagmite, and the presence of more reversals lower down, suggest that this is not a reliable stalagmite that can guarantee a sufficient number of data points in the last 500 years.	

DP1	Dante, Namibia	17°53 E, 19°24 S	<p>The stalagmite has 6 reddish-brown horizons that, when viewed in a thin section, contain detrital clays and/or iron oxides. One of these thin horizons was penetrated by sample DP1-450 and had a <math>^{232}\text{Th}</math> concentration 54 times that of the mean of all the other samples. Furthermore; “few surfaces in DP1 have void spaces analogous to Type E surfaces. These surfaces feature thin detrital layers below which are irregular voids in aragonite, suggesting that dripwaters deposited a detrital material and then dissolved the underlying stalagmite” (Sletten, 2013)</p> <p>The variety of issues with stalagmite DP1 have led to it being disqualified from the <math>^{232}\text{Th}</math>/DCMD correlation curve.</p>	
-----	-------------------	---------------------	--	---

20120824-13	Yelang, China	105°44 E, 26°2 N	The analytical precision of the samples taken from this stalagmite are described as “very poor” by M. Zhao et al. (2017) in their paper. Combined with some porous/iron-stained layers between 300- and 800-years BP, this stalagmite has been deemed unreliable and removed from the correlation curve.	 <p>Calibrated <sup>14</sup>C age (Kyr BP)</p> <p>20120824-13 <sup>230</sup>Th/U dates</p> <p>Depth from the top (mm)</p> <p>Mid-Holocene to Late Holocene gap</p> <p>LGM gap</p> <p>393±87</p> <p>771±68*</p> <p>3395±1023</p> <p>9514±2896</p> <p>218689±2611</p> <p>8785±408</p> <p>10938±435</p> <p>10614±135</p> <p>47103±591</p> <p>48332±8159</p> <p>93166±2697</p>
ALH06	Pau d'Alho, Brazil	56°48'41 W, 15°12'20 S	The magnetite data extracted from ALH06 formed a tight cluster and overlap the field of detrital magnetite (on an MDF/DP plot) (Jaqueto, 2016). Furthermore, magnetic data obtained on soils and cave sediments are identical in acquisition curves of IRM and ARM. For this reason, we believe that <sup>232</sup> Th concentrations measured in stalagmite ALH06 are not representative of atmospherically entrained dust but instead originate from local soil.	NA

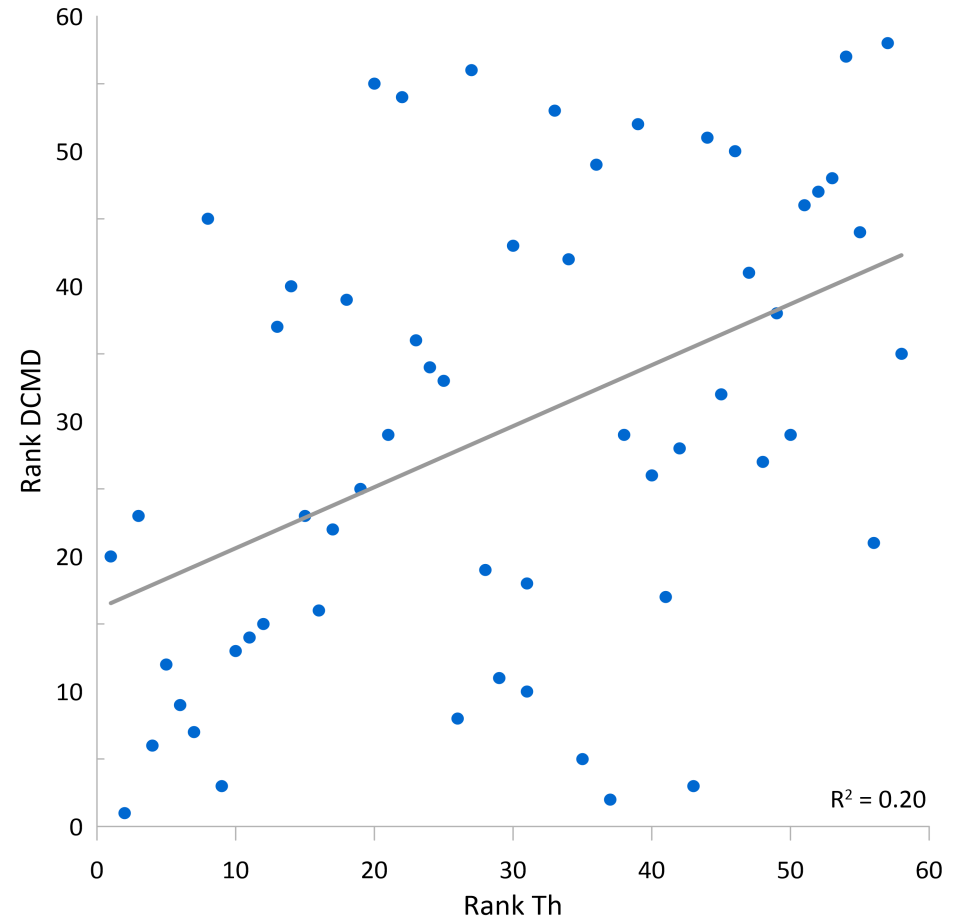
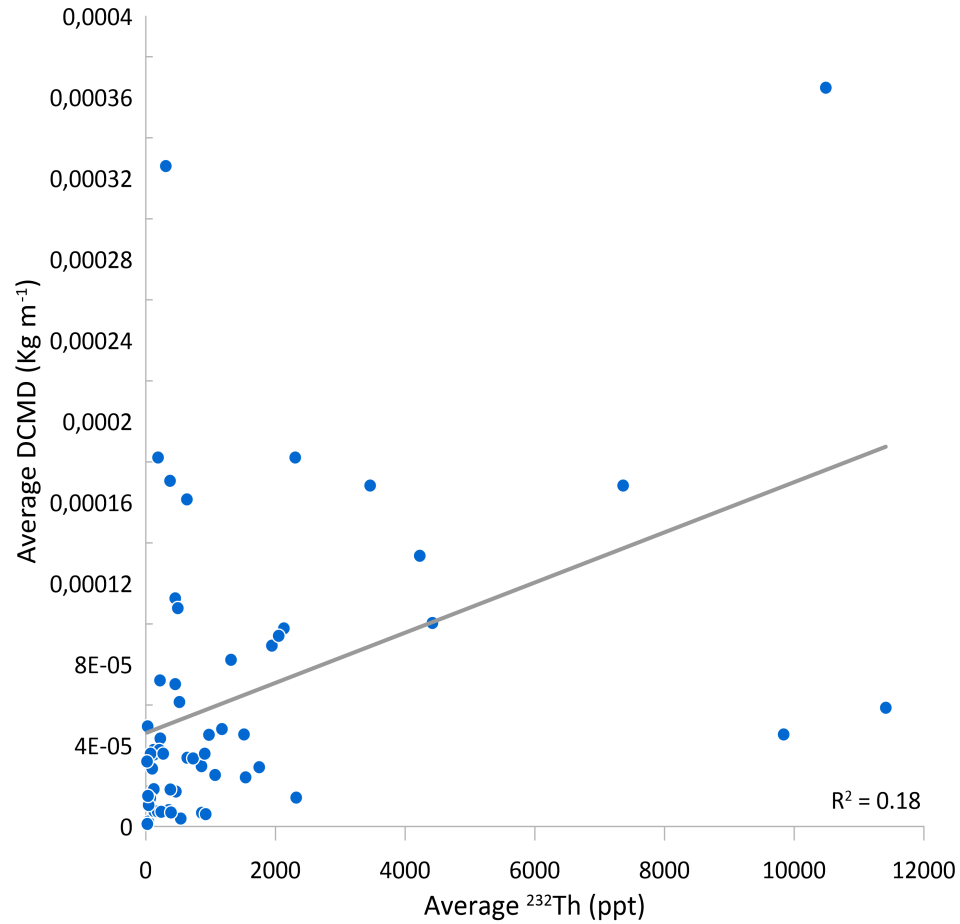
<p>MC01</p>	<p>Macal Chasm, Belize</p>	<p>89.108°W, 16.883°N</p>	<p>Discontinuous dark layers brought the reliability of this speleothem record into question (see column 5). If this coloration was representative of atmospheric dust fluxes at the time of laminae precipitation, it would be expected to extend laterally throughout the laminae.</p>	
<p>TUL</p>	<p>Chulerasim, India</p>	<p>79°21'06 E, 29°53'08 N</p>	<p>The scan presented in Kotlia et al.'s (2013) publication (column 5), shows discontinuous darker layers. In combination with high age errors, this stalagmite is believed to be unreliable in a study correlating <math>^{232}\text{Th}</math> isotope concentrations and atmospheric dust.</p>	

IFK1	Ifoulki, Morocco	09°19'39 W, 30°42'29' N	<p>This is a very valuable stalagmite to the study because of its geographical location, and the lack of other stalagmite records in Saharan Africa. However, it has been removed due to inconsistencies in laminae coloration. Darker layers do not extend from the growth axis to the outer edge of the stalagmite. Consistent application of this rule means that the IFK1 stalagmite is also disqualified from the record.</p>	
ZJD-21	Zhijin, China	NA	<p>Stalagmite ZJD-21 has been removed from the correlation curve due to random staining and porosity which we believe do not track changes in dust flux reliably. See column 5.</p>	

P00-H1	Huagapo, Peru	75°79 W, 1°27 S	Apparently random, green staining throughout the stalagmite, in combination with the risk of periodic flooding events (due to the stream flowing along the cave floor year-round), made the record seem unreliable. The decision was made to not include this stalagmite in the study and instead to opt for other more reliable records.	 <p>The figure shows a photograph of a stalagmite labeled P00-H1 on the left. To its right is a graph with 'Depth from Top (mm)' on the y-axis (0 to 120) and 'Years (BP 1950)' on the x-axis (0 to 2000). A series of data points connected by a line shows a linear relationship, indicating a constant growth rate. The points are approximately at (0, 0), (20, 10), (40, 20), (60, 30), (80, 40), (100, 50), (120, 60), (140, 70), (160, 80), (180, 90), (200, 100), (220, 110), (240, 120).</p>
C11	Cueva del Cobre, Spain	NA	The top of the stalagmite appears to be stained with a material that is not present throughout the lower portions of the sample. There is also some lateral discontinuity of coloration, which has been described in other disregarded stalagmites. Martin-Chivelet et al. (2011) describe the passage from which C11 was removed as “a small remote passage located more than 1 km away from the mainentrance, an area of negligible air current”. The combination of these three factors have led to the decision to remove stalagmite C11 from the correlation curve.	 <p>The figure shows a photograph of a stalagmite labeled C11. A white arrow points to a dark stain at the top of the stalagmite. The label 'b' is in the top left corner of the image area, and 'C11' is at the bottom.</p>

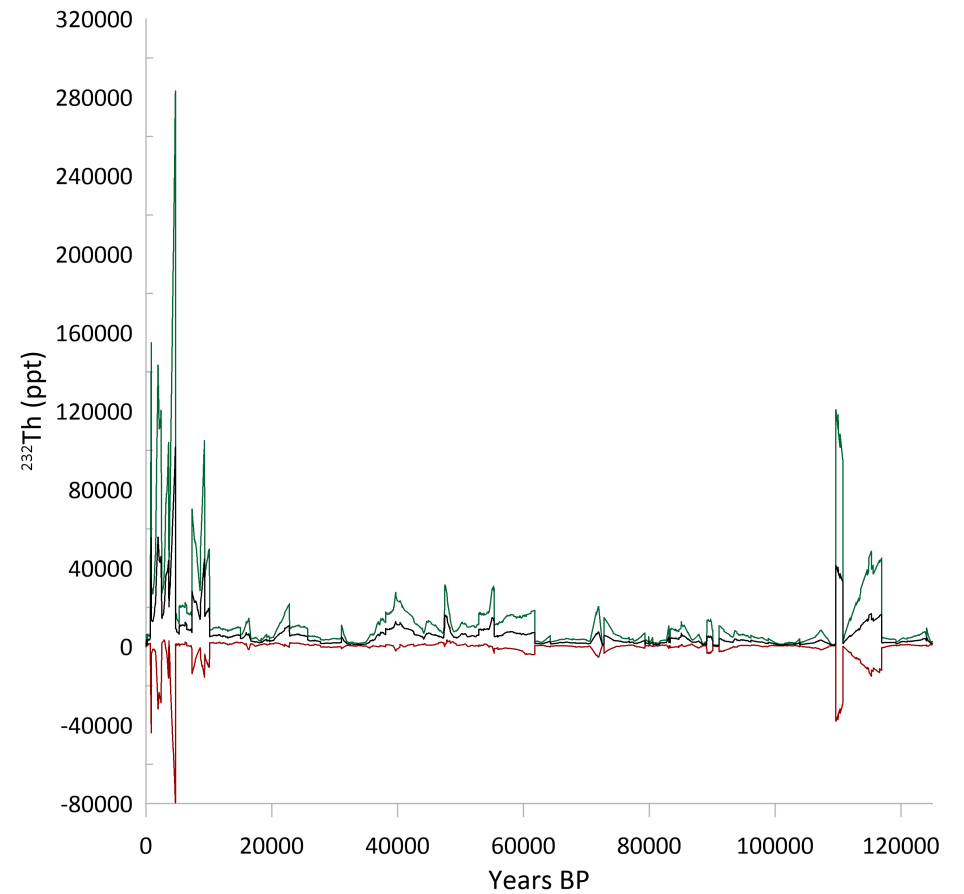
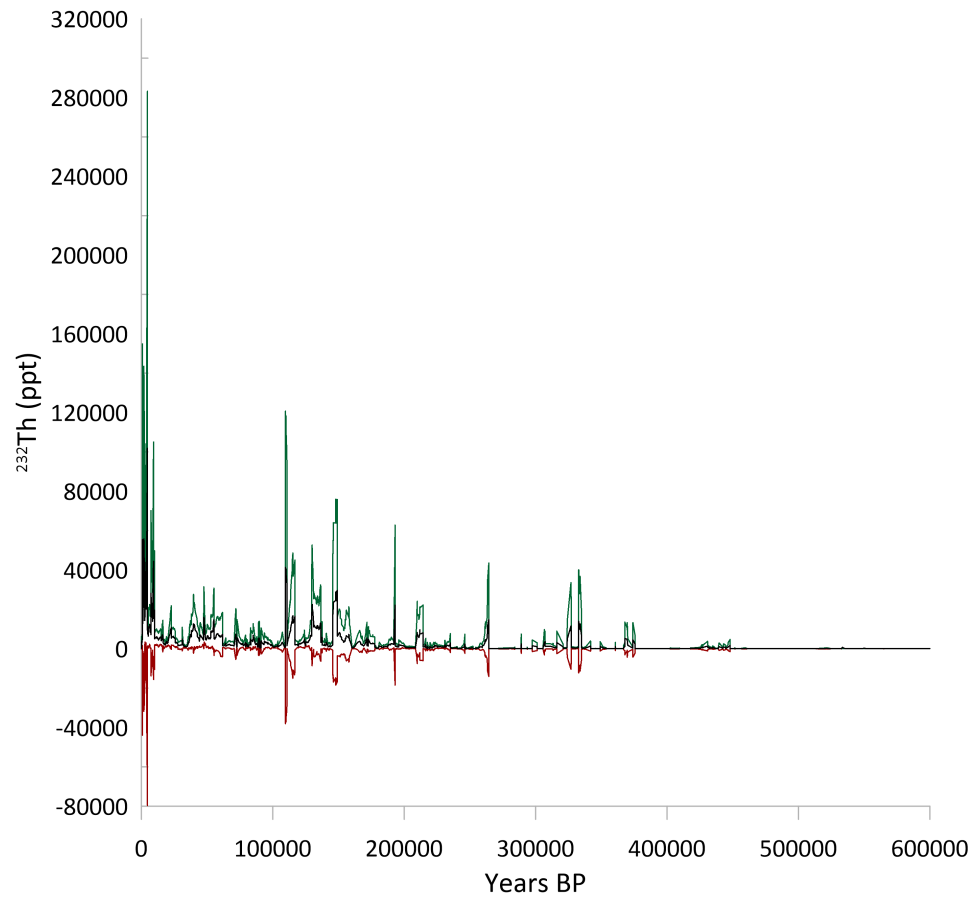
## Appendix 5

Pearson (left) and Spearman (right) plots illustrating the correlation between mean  $^{232}\text{Th}$  values over the last 500 years and mean, modern DCMD values taken from an area of  $1^\circ$  of latitude and longitude squared around the cave sites, including disregarded stalagmite data points listed in Appendix 4 above.



## Appendix 6

Time series plot illustrating the mean  $^{232}\text{Th}$  concentrations from the compiled stalagmite record (black). Upper (green) and lower (red) limits of the confidence interval were calculated based on the standard deviation and sample size for each 10-year interval. Plot b) highlights the period between 0-120 ka that this study focusses on.





Appendix 7

Time series plot illustrating compiled  $\delta^{18}\text{O}$  curves from stalagmites found in Kesang (violet) and TON (orange) caves during the late Pleistocene. Long linear sections indicate extended periods of interpolation.

